A&A 606, A86 (2017)
DOI: 10.1051/0004-6361/201730609
© ESO 2017

Astronomy & Astrophysics

Interstellar medium conditions in $z \sim 0.2$ Lyman-break analogs

A. Contursi[1], A. J. Baker[2], S. Berta[1,10,⋆], B. Magnelli[3], D. Lutz[1], J. Fischer[4], A. Verma[5], M. Nielbock[6], J. Grácia Carpio[1], S. Veilleux[7], E. Sturm[1], R. Davies[1], R. Genzel[1], S. Hailey-Dunsheath[8], R. Herrera-Camus[1], A. Janssen[1], A. Poglitsch[1], A. Sternberg[9], and L. J. Tacconi[1]

[1] Max-Planck-Institut für extraterrestrische Physik, Postfach 1312, 85741 Garching, Germany
e-mail: contursi@mpe.mpg.de
[2] Department of Physics and Astronomy, Rutgers, The State University of New Jersey, 136 Frelinghuysen Road, Piscataway, NJ 08854-8019, USA
[3] Argelander-Institut für Astronomie, Universität Bonn, Auf dem Hügel 71, 53121 Bonn, Germany
[4] Naval Research Laborratory, Remote Sensing Division, 4555 Overlook Ave SW, Washington, DC 20375, USA
[5] Oxford University, Dept. of Astrophysics, Oxford OX1 3RH, UK
[6] Max-Planck Institut für Astronomie, Königstuhl 17, 69117 Heidelberg; Universität Heidelberg, Zentrum für Astronomie, Inst. für Theor. Astrophysik, Albert-Ueberle-Str. 2, 69120 Heidelberg, Germany
[7] Department of Astronomy and Joint Space Science Institute, University of Maryland, College Park, MD 20742, USA
[8] California Institute of Technology, 301-17, 1200 E. California Blvd., Pasadena, CA 91125, USA
[9] Tel Aviv University, Sackler School of Physics & Astronomy, 69978 Ramat Aviv, Israel
[10] Department of Physics, Faculty of Science, University of Zagreb, Bijenička cesta 32, 10000 Zagreb, Croatia

Received 13 February 2017 / Accepted 12 June 2017

ABSTRACT

We present an analysis of far–infrared (FIR) [CII] and [OI] fine structure line and continuum observations obtained with *Herschel*/PACS, and ^{12}CO(1–0) observations obtained with the IRAM Plateau de Bure Interferometer, of Lyman-break analogs (LBAs) at $z \sim 0.2$. The principal aim of this work is to determine the typical interstellar medium (ISM) properties of $z \sim 1$–2 main sequence (MS) galaxies, with stellar masses between $10^{9.5}$ and 10^{11} $M_\odot$, which are currently not easily detectable in all these lines even with ALMA and NOEMA. We perform PDR modeling and apply different infared diagnostics to derive the main physical parameters of the far-infrared (FIR)-emitting gas and dust and we compare the derived ISM properties to those of galaxies on and above the MS at different redshifts. We find that the ISM properties of LBAs are quite extreme (low gas temperature and high density and thermal pressure) with respect to those found in local normal spirals and more active local galaxies. LBAs have no [CII] deficit despite having the high specific star formation rates (sSFRs) typical of starbursts. Although LBAs lie above the local MS, we show that their ISM properties are more similar to those of high-redshift MS galaxies than of local galaxies above the main sequence. This data set represents an important reference for planning future ALMA [CII] observations of relatively low-mass MS galaxies at the epoch of the peak of the cosmic star formation.

Key words. galaxies: evolution – galaxies: ISM – galaxies: high-redshift – infrared: galaxies

1. Introduction

In the last decade, increasing observational and theoretical studies at low and high redshift have shown that the conditions of the interstellar medium (ISM) in galaxies have a primary role in their evolution. In the stellar mass (M_*) versus star formation rate (SFR) plane, star-forming galaxies (SFGs) at all redshifts sampled so far (up to $z \sim 6$. Salmon et al. 2015) follow a tight correlation called the main sequence (MS) such that the SFR increases with redshift for a given stellar mass. Nevertheless, at a given stellar mass, the efficiency of star formation (i.e., the SFR per unit of molecular gas mass) is broadly constant for MS galaxies at all redshifts, and the increase of the SFR with z is primarily driven by an increasingly high gas fraction (Daddi et al. 2010b; Saintonge et al. 2011; Tacconi et al. 2010, 2013; Genzel et al. 2015).

Observations have also shown that the gas distribution and dynamical state of MS galaxies evolves with redshift. Kinematic and dynamical studies of the ionized and molecular gas in MS SFGs at the epoch where the cosmic star formation peaks, that is, $z = 2$–3, have shown that by this time the more massive MS galaxies have already formed regularly rotating disks similar to those of local star-forming galaxies. However, the gas is clumpier and has a higher velocity dispersion than the gas in local MS galaxies (Wisnioski et al. 2015). Thus, the ISM dynamical state, the gas content, and the rate at which a galaxy is turning gas into stars are amongst the fundamental parameters that regulate the evolution of a galaxy.

Most previous studies of the ISM in high-redshift galaxies have analyzed ionized and molecular gas. The cold neutral atomic medium is another important phase of the ISM in galaxies, and its study can provide complementary information on the physical conditions in the ISM and hence on galaxy evolution. One way to study this phase of the ISM is with observations of the [CII] ($^2P_{1/2} \rightarrow {}^2P_{3/2}$) line at 157.7 μm and the [OI] ($^3P_2 \rightarrow {}^3P_1$) line at 63.2 μm, the most luminous far-infrared (FIR) fine structure lines; in local SFGs these lines represent 0.1–1% of the FIR luminosity (Malhotra et al. 2001; Graciá Carpio et al. 2011). These lines are the major coolants of the ISM, and therefore they are very important for the energetic balance of the ISM.

⋆ Visiting scientist.

The recent availability of new sensitive submillimeter interferometers has opened up the possibility of observing [CII] in high-redshift galaxies (Carilli & Walter 2013) where observation of the HI hyperfine line at 21 cm is not yet possible. However, these observations are still challenging at $z = 2$–3, and so far restricted to the most luminous and massive systems (QSOs, submillimeter galaxies, massive MS galaxies). What is ultimately needed is the study of the cold atomic gas in high-redshift MS SFG samples matching those already studied in ionized and molecular gas.

An ideal sample is represented by the Lyman break galaxies (LBGs, Steidel et al. 1996), selected using color criteria sensitive to the presence of a Lyman continuum break in an otherwise very blue rest far-UV continuum in the redshift range $z \sim 2$–3. LBGs have been extensively studied at many wavelengths and represent an obvious population to be observed in the [CII] line. However, observations of such relatively low-infrared-luminosity systems at high redshift are still very difficult even with the state–of–the–art receivers of modern submillimeter interferometers.

In order to study the ISM conditions in such systems in more detail, we have undertaken a program to observe a small sample of local ($z \sim 0.2$) analogs of LBGs (Lyman–break analogs or LBAs; Heckman et al. 2005, 2011; Hoopes et al. 2007; Overzier et al. 2008, 2009, 2010, 2011; Basu-Zych et al. 2007, 2009; Gonçalves et al. 2010) in [CII] and [OI] line emission as well as in FIR continuum emission. Our study uses the PACS spectrometer and photometer (Poglitsch et al. 2010) on–board the *Herschel* satellite (Pilbratt et al. 2010) as part of a guaranteed–time program (P.I. A. Contursi). We also present ^{12}CO(1–0) IRAM Plateau de Bure (PdBI) observations of some of our targets in order to extend our analysis to their molecular gas. With this work, we aim also to provide a unique reference for designing ALMA [CII] and continuum observations of SFGs at the epoch where cosmic star formation peaks.

The paper is organized as follows. In Sect. 2, we introduce the sample. In Sect. 3, we describe the data reduction and the extraction of the line and continuum fluxes. The derivation of the main parameters necessary for the analysis is given in Sect. 4. In Sect. 5, we present the main results obtained by modeling the FIR fine structure lines. In Sect. 6, we discuss these results in the framework of galaxy evolution. A summary of the results and conclusions are given in Sect. 7.

2. The sample

2.1. Lyman-break analogs

LBAs are ultra-compact UV luminous galaxies at redshift $z \sim 0.1$–0.3 selected to have $L_{\rm UV} > 2 \times 10^{10}\ L_\odot$ and very high UV surface brightness $I_{1530\ \text{Å}} > 10^9\ L_\odot\ \text{kpc}^{-2}$ (Heckman et al. 2005). With UV half-light radii between 0.5 and a few kpc (Overzier et al. 2010), they are more compact and have higher SFR per unit area than large UV-bright local spirals (Hoopes et al. 2007). They are more luminous than blue compact dwarfs in the UV and are much more rare. Their SFRs span from ~3 to 100 $M_\odot\ \text{yr}^{-1}$, and their specific SFRs (sSFRs) are higher than those of large UV-bright galaxies. Overzier et al. (2009) propose that LBAs could represent a very short, relatively unobscured evolutionary phase of a starburst. Several of these galaxies show disturbed morphologies and tails, indicating signs of interactions, with generally disk-like structures featuring compact luminous clumps. Some LBAs are dominated by very UV-bright, compact (~10^2 pc), and massive (~$10^9\ M_\odot$) clumps. These galaxies are called "Dominant Central Objects" (DCOs) and exhibit higher sSFR than the rest of the sample (Overzier et al. 2009). Some DCOs also show clear signs of high-velocity ionized gas outflows (~400 km s^{-1} < v < 1500 km s^{-1}) and a high percentage (up to ~40%) of escaping Lyman continuum photons thanks to a clumpy neutral medium (Heckman et al. 2011).

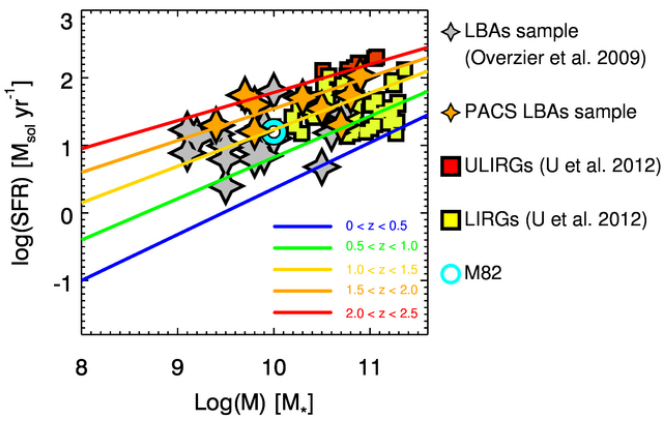

Fig. 1. Location of LBAs on the *SFR*-M_* plane. Diamonds correspond to the sample of Overzier et al. (2009). Orange diamonds represent the subsample presented in this work. SFRs and stellar masses are from Overzier et al. (2009). SFRs are calculated from Hα + 24 μm flux assuming a Kroupa IMF. The sample of ULIRGs (red) and LIRGs (yellow) is taken from U et al. (2012). The overplotted lines are the relationships followed by star-forming galaxies at different redshifts presented in Whitaker et al. (2012), who use a similar derivation for the SFR. The position of the typical local starburst galaxy M 82 is also shown for reference.

LBAs and LBGs share many properties, including their ranges of UV luminosity and surface brightness, morphology, stellar mass, SFR and metallicity. LBAs, like LBGs, suffer less attenuation than local galaxies with the same bolometric luminosities (Overzier et al. 2011). In the IR/UV versus the stellar mass plane, LBAs lie well below the relation followed by local SDSS galaxies. LBAs also follow three fundamental scaling relations that further show their similarity to LBGs. First, in the stellar mass/metallicity relation shown in Fig. 9 of Hoopes et al. (2007; we refer also to Lian et al. 2015), LBAs follow the mass-metallicity relation of $z \sim 2$ UV star-forming galaxies (Erb et al. 2006b). There is also some overlap between LBAs and local (Ultra) Luminous Infrared Galaxies ((U)LIRGs), but LBAs have, on average, lower metallicities (sub-solar) than (U)LIRGs (1–2 × $Z_\odot$ Inami et al. 2013), and lower extinction. Second, Overzier et al. (2009) show that LBAs have [N II]/Hα ratios higher than those of nearby warm IR galaxies with the same [O III]/Hβ ratio (Baldwin et al. 1981; Veilleux & Osterbrock 1987, BPT), but similar to the ratios of a variety of $1 < z < 2.5$ star-forming galaxy samples (Steidel et al. 2014). This suggests similar conditions in the ionized gas for LBAs and high-z galaxies. The LBAs that occupy the composite HII-AGN region of the BPT diagram are also DCOs. There is no clear evidence that these galaxies host hidden AGN, except for SDSS092159, which most likely hosts a black hole with a mass $\leq 10^7\ M_\odot$ (Alexandroff et al. 2012). This does not exclude the presence of low-luminosity AGN in the other composite sources, but if AGNs are present, they do not dominate the emission. Third, Fig. 1 shows the original sample of LBAs from Overzier et al. (2009) in the *SFR*-M_* plane. The subsample of galaxies presented in this work is shown in orange diamonds (we refer to

Table 1. The sample observed with the PACS photometer and spectrometer.

#	Name	RA J2000	Dec J2000	z	$\log M_*$ ($M_\odot$)	Z^+	SFR ($M_\odot$/yr) Hα + 24 μm	$\log L_{24}$ ($L_\odot$)	$\log L_{70}$ ($L_\odot$)
1	005527	00:55:27.46	–00:21:48.71	0.16744**	9.7	8.28	55.4	10.8	11.12
2	015028†	01:50:28.41	13:08:58.40	0.14668**	10.3	8.39	50.7	10.8	11.47
3	021348†	02:13:48.54	12:59:51.46	0.21902**	10.5	8.74	35.1	10.7	–
4	080844	08:08:44.27	39:48:52.36	0.09123**	9.8	8.74	16.1	10.3	10.53
5	082001	08:20:01.72	50:50:39.16	0.217	9.8	8.15	40.0	10.6	11.00
6	092159	09:21:59.39	45:09:12.38	0.23499**	10.8	8.67	55.1	10.8	11.60
7	093813	09:38:13.50	54:28:25.09	0.10208**	9.4	8.19	19.8	10.2	10.54
8	143417†	14:34:17.16	02:07:42.58	0.180	10.7	8.65	20.0	10.1	10.86
9	210358†	21:03:58.75	–07:28:02.45	0.13698**	10.9	8.70	108.3	11.1	11.35

Notes. Data are from Overzier et al. (2009) except for updated redshifts when available (**) from Heckman et al. (2011). $^{(+)}$ 12 + log(O/H) estimated using the O3N2 estimator from Pettini & Pagel (2004). $^{(\dagger)}$ CO available.

Table 2. Classification and morphological properties of the LBA sample presented in this work.

Name	DCO^a	Interacting /merger^b	Ionized gas $v_{\rm max}^{\rm Outflow\,c}$ km s^{-1}	High % escape fraction^c	BPT^a classification	AGN^a signatures
005527	no	no	–640	no	HII	no
015028	no	tidal?	–480	no	HII	no
021348	yes	–	–1500	yes	Comp.	no
080844	yes	companion	–1500	yes	Comp.	no
082001	no	no	–	no	Comp.	no
092159	yes	–	–1500	no	HII	yes
093813	no	merger	–610	yes	HII	no
143417	no	interaction	–	no	Comp.	no
210358	yes	no	–1500	no	Comp.	no

Notes. We also report the percentage of the Lyman continuum leakage that indicates the presence of a clumpy neutral phase, that we study in this work. $^{(a)}$ Overzier et al. (2009); $^{(b)}$ Gonçalves et al. (2010); $^{(c)}$ Heckman et al. (2011).

the following section for the sample selection criteria). For comparison, we plot a sample of ULIRGs and LIRGs from U et al. (2012), the position of the local starburst M82, and the main sequence at different redshifts as published by Whitaker et al. (2012). LBAs lie above the local SFR-M_* relation followed by normal star-forming galaxies. The LBAs we have selected to be observed with PACS are LIRGs, and, in fact, they overlap in part with the LIRGs sample of U et al. (2012), but are, on average, less massive and have lower metallicities and IR/UV ratios.

2.2. Target selection

We selected nine LBAs from the Overzier et al. (2009) sample based on two criteria: (1) the redshift must be such that the [CII] line falls at a wavelength lower than 196 μm, beyond which the leakage from the second order makes the flux calibration very uncertain; and (2) the IR continuum emission must be bright enough to reach $S/N \gtrsim 10$ in a reasonable amount of time with PACS (not more than 3 h per line per source).

Table 1 lists the selected targets with their main characteristics from Overzier et al. (2009) and Basu-Zych et al. (2007). We observed all nine targets in [CII] and five of the nine in the 63 μm [OI] line. We observed all nine targets with the PACS photometer in the green (100 μm) and red (160 μm) broadband filters. Since LBAs have been extensively studied at many wavelengths in previous works, many of their properties are already known for all targets. We summarize the most important of these in Table 2.

Figure 1 shows that our sample (orange diamonds), despite being small and not complete, spans most of the parameter space covered by the original sample of Overzier et al. (2009; gray diamonds), although is biased towards slightly higher SFR and stellar mass.

By complementing the FIR data with IRAM PdBI ^{12}CO(1–0) observations of four targets presented here for the first time, and with CARMA ^{12}CO(1–0) data available for two additional galaxies from Gonçalves et al. (2014), we are able to probe the neutral atomic and molecular gas and dust content of LBAs.

3. Observations and data reduction

3.1. PACS data

We list the details of all PACS observations in Table 3. All spectrometer observations were executed in chop–nod line (small range) scan mode for [CII] ([OI]). The [OI] integration times were typically four times longer than those of [CII], often approaching one hour. The spectrometer data have been reduced in HIPE[1] using the telescope background normalization method. This method does not use the calibration block executed at the beginning of the observations to flux–calibrate the spectrum, but instead uses the telescope background spectrum itself. The advantage is that in this case, each chop on-off calculation is normalized to the sum of chop on plus chop off, resulting in

[1] HIPE is a joint development by the Herschel Science Ground Segment Consortium, consisting of ESA, the NASA *Herschel* Science Center, and the HIFI, PACS and SPIRE consortia.

Table 3. PACS photometer and spectrometer observational details.

Name	Line/band	OBSID	Time on source (s)
005527	[CII]	1342213130	860
	[OI]	1342213315	3920
	Green+red	1342222493/4	180
015028	[CII]	1342213912	860
	[OI]	1342213750	3920
	Green+red	1342223572/3	180
021348	[CII]	1342213911	3440
	Green+red	1342223654/5	360
080844	[CII]	1342220752	860
	[OI]	1342220141	2800
	Green+red	1342220125/6	180
082001	[CII]	1342220751	3440
	Green+red	1342220121/2	360
092159	[CII]	1342221362	3440
	Green +red	1342220657/8	180
093813	[CII]	1342221632	860
	[OI]	1342221631	2800
	Green+red	1342220661/2	180
143417	[CII]	1342213757	3440
	Green+red	1342223838/9	360
210358	[CII]	1342208937	860
	[OI]	1342221358	3840
	Green+red	1342218538/9	180

a signal normalized to the telescope background emission for every chopping cycle, thereby correcting the responsivity drifts much more efficiently and at much higher temporal sampling than is done with the calibration block reduction. This method is particularly recommended for long observations (such as ours), and it also usually works better in recovering baselines when targets are very faint or, for point sources, where the continuum flux is expected to be zero. We have verified that our targets are all point sources at all wavelengths with respect to the PACS beams (FWHM from 9 to 13″) in agreement with their UV and optical extension of $\lesssim$5″ (Gonçalves et al. 2010).

To extract a point-source flux, there are two methods. One consists of extracting the spectrum from the central spaxel only and applying a point source correction loss to recover the total flux. This offers the advantage that the spectrum of the central spaxel has the highest S/N. However, if the observation is significantly mispointed ($\gtrsim$3″), one can sum the signal of the central 3 × 3 spaxels and apply a correction from this to the total flux, thus reducing the effect of any possible mispointing. The disadvantage with this method is that if the signal is faint, as is the case for most of our targets, summing the central nine spaxels increases the noise.

Given the latter consideration, we have chosen to extract the final source spectra using the central spaxel for all targets except when the mispointing is evident from the 5 × 5 spaxel flux distribution. This is the case for two galaxies, SDSSJ210358 and SDSSJ015028, in which the [CII] and [OI] lines, which should arise in the same gas, appear spectrally misaligned. In fact, when a target is mispointed in a direction perpendicular to the slices, spectra are artificially skewed, and thus their line profiles, and hence velocity peaks and widths, are altered (we refer to Fig. 14.18 of the PACS spectroscopy Calibration Document[2]).

[2] http://herschel.esac.esa.int/twiki/pub/Public/PacsCalibrationWeb/PacsSpectroscopyPerformanceAndCalibration_v2_4.pdf

Table 4. Continuum flux densities and uncertainties calculated from the maps observed with the PACS photometer (in bold and with superscript p), and from the continuum values on both sides of the lines and from the parallel channels of the spectrometer observations (s).

Name	λ μm	Flux density mJy
005527		
	73.76^s	152.5 ± 78.7
	92.11^s	178.0 ± 145.0
	100.00^p	**109.9 ± 10.9**
	147.52^s	77.3 ± 25.9
	160.00^p	**76.7 ± 18.2**
	184.17^s	103.7 ± 193.1
015028		
	72.50^s	494.6 ± 78.8
	90.49^s	575.9 ± 146.2
	100.00^p	**487.4 ± 20.3**
	145.03^s	339.6 ± 23.0
	160.00^p	**334.1 ± 14.2**
	180.87^s	404.7 ± 192.837
021348	96.18^s	145.4 ± 83.2
	100.00^p	**302.36 ± 5.5**
	160.00^p	**211.2 ± 16.3**
	192.28^s	91.2 ± 98.4
080844	68.95^s	145.7 ± 70.6
	86.09^s	270.9 ± 161.7
	100.00^p	**200.7 ± 135.1**
	137.95^s	200.5 ± 33.9
	160.00^p	**146.3 ± 110.2**s
	172.10^s	262.2 ± 143.7
082001	96.04^s	64.6 ± 119.1
	100.00^p	**68.7 ± 10.0**
	160.00^p	**67.54 ± 5.0**
	191.99^s	4.7 ± 116.603
092159	97.41^s	61.2 ± 125.8
	100.00^p	**264.59 ± 7.7**
	160.00^p	**214.09 ± 11.5**
	194.75^s	95.4 ± 101.6
093813	69.66^s	102.2 ± 65.3
	86.95^s	195.9 ± 159.4
	100.00^p	**130.3 ± 6.8**
	139.35^s	81.3 ± 14.8
	160.00^p	**77.0 ± 7.1**
	173.82^s	115.5 ± 137.2
143417	93.14^s	76.3 ± 82.51
	100.00^p	**103.9 ± 8.3**
	160.00^p	**89.0 ± 15.0**
	186.26^s	47.6 ± 110.809
210358	71.87^s	419.9 ± 102.5
	89.697^s	621.7 ± 152.3
	100.00^p	**603.8 ± 8.2**
	143.80^s	567.1 ± 18.3
	160.00^p	**508.4 ± 26.2**
	179.32^s	551.2 ± 147.6

Notes. The uncertainties are the measured rms.

For these two galaxies, we extract the sum of the 3 × 3 central spaxels to recover the line profiles more correctly.

The nominal flux uncertainties (~10%) reported in the PACS spectrometer calibration document are strictly valid only for continuum flux $\gtrsim$1 Jy. In the much fainter regime of emission of our targets, uncertainties are likely to be higher. Taking all these facts together, we estimate our flux uncertainties for the lines to be ~25%.

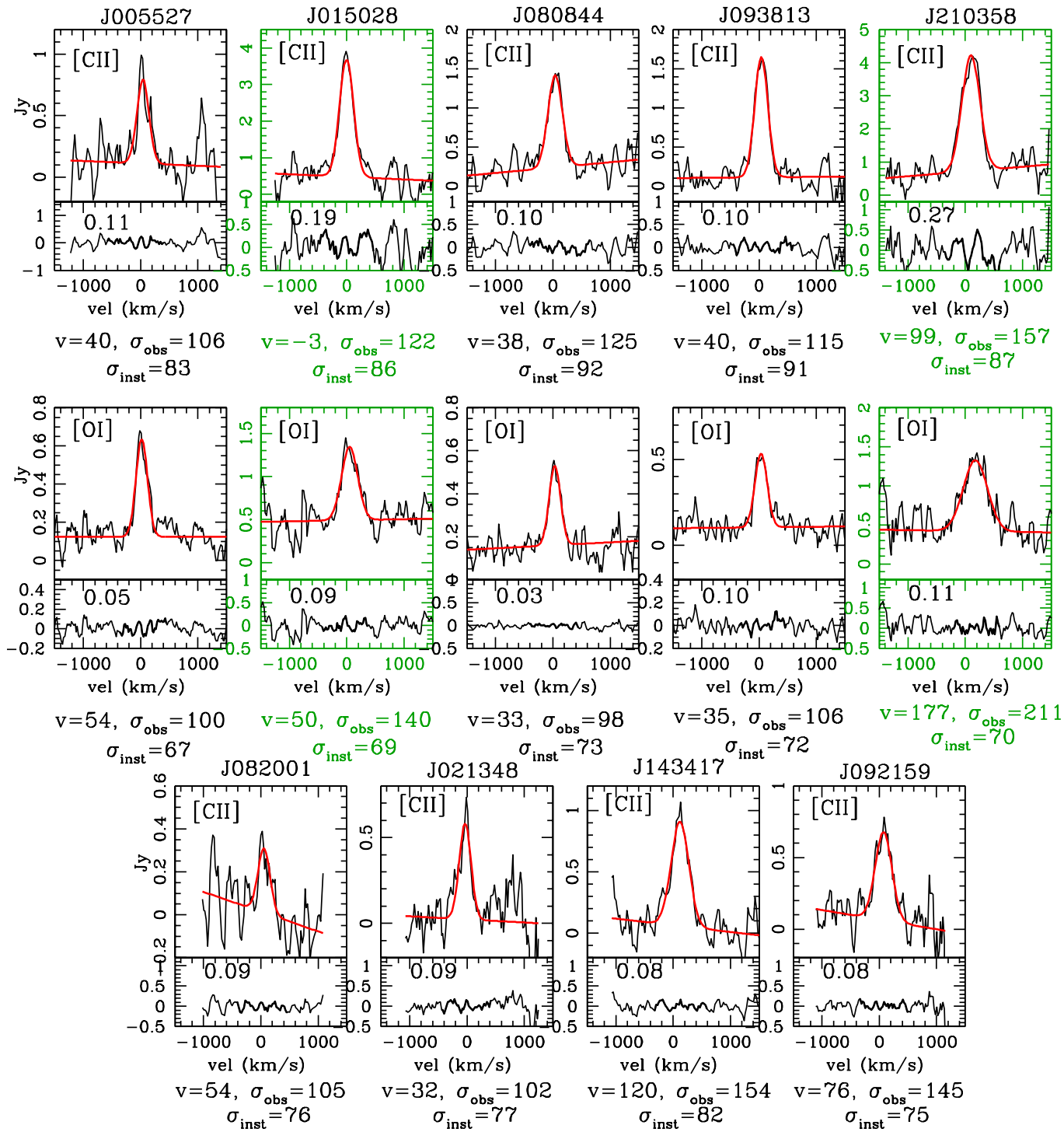

Fig. 2. PACS spectra of all targets in km s^{-1}. Zero velocity corresponds to the redshift listed in Table 1. Each black or green frame contains the single Gaussian fit for [CII] (*upper*) and [OI] (*lower* when available) and residuals for each target. We report the fitted peak velocities, velocity dispersion $\sigma_{\rm obs}$ and instrumental $\sigma_{\rm inst}$ at the observed wavelength in km s^{-1}. Black frames refer to spectra extracted from the central spaxel with the Point Source Correction; green frames refer to extraction from the sum of the central nine spaxels with the Point Source Correction, to correct for line distortion introduced in badly pointed data (we refer to the text for details).

All photometer observations were executed in small scan mode with two scan directions in the green and red filter. We reduced them with the standard pipeline and extract fluxes by using aperture photometry and applying the point-source corrections. We have also derived the continuum flux densities from the spectrometer data on either side of the targeted lines and in the corresponding parallel channels. The errors on the continuum fluxes measured from the spectra are in general higher than those at the line centers because the sampling is lower there. Table 4 lists the continuum flux densities derived from the photometer and the spectrometer data.

[CII] and [OI] fluxes and line profiles. Figure 2 shows the observed spectra as a function of velocity in km s^{-1}, relative to the optical systemic velocity listed in Col. 5 of Table 1.

Table 5. Line fluxes and S/N calculated from the central spaxel with point source correction for all galaxies except for those denoted with an asterisk, which have been extracted from the central nine (see text for details).

#	Name	[CII] 10^{-18} W m^{-2}	S/N	[OI] 10^{-18} W m^{-2}	S/N	[CII] $FWHM_{\rm obs}$ (instr) km s^{-1}	[OI] $FWHM_{\rm obs}$ (instr) km s^{-1}
1	005527	11.6	5.3	20.4	4.0	156.3 (196.1)	175.5 (159.2)
2	015028*	62.5	21.5	47.4	7.5	206.3 (202.0)	287.2 (162.3)
3	021348	9.0	22.5	–	–	159.7 (180.7)	–
4	080844	23.5	12.0	14.5	4.3	199.3 (216.8)	156.2 (17 1.3)
5	082001	< 5.0	–	–	–	<169.6 (181.2)	–
6	092159	14.2	14.5	–	–	194.2 (175.4)	–
7	093813	28.1	10.5	18.0	4.3	166.0 (214.0)	183.0 (169.5)
8	143417	20.8	5.2	–	–	307.4 (192.3)	–
9	210358*	87.4	40.5	76.0	14.0	307.7 (159.2)	402.6 (263.9)

Notes. The last two columns list the intrinsic line and instrumental FWHMs at the observed wavelengths obtained from the single Gaussian fit. The uncertainties in the line fluxes are ~25% (see text for details).

Both [CII] and [OI] lines were detected in all galaxies except in SDSSJ082001, which shows a marginal detection in [CII] (it was not observed in [OI]) that we treat as an upper limit.

The spectra were extracted as explained in Sect. 3.1. For each target we show fits to a single Gaussian plus linear baseline model and the corresponding residuals at the bottom of each spectrum. In each residual panel, we show the standard deviation calculated in the spectral region indicated with a thicker line. We also report the fitted velocity peak, the observed line dispersion and the instrumental dispersion at the observed wavelength in km s^{-1}. Taking into account all uncertainties due to the nominal wavelength calibration and to the line profile changes introduced by mispointing, we estimate that the overall uncertainty in velocity is ~50 km s^{-1} in both lines.

The fitted parameters of the two lines marginally agree for galaxy SDSSJ015028 but differ by more than the uncertainties for galaxy SDSSJ210358. The spectra of the latter galaxy clearly show two components, so we fit both [CII] and [OI] with two Gaussian components plus a linear continuum, and we obtain better agreement between the peak velocities for both components for the two lines. This is shown in Fig. 3, where it is also clear that the dispersion of the residuals is much lower than that obtained in the case of one fit component.

For completeness, we have also performed double Gaussian fits for all targets, to explore the presence of multiple or broad components, but we do not obtain improvement in the fits. This result, however, does not rule out the existence of broad wings indicating outflowing neutral atomic gas, given the low S/N. Table 5 lists the line flux, the S/N, and the instrumental and observed FWHMs derived from the single-Gaussian fits.

We clearly resolve the lines in SDSSJ143417, SDSS092159, SDSSJ210358 and SDSSJ015028. The other targets show line widths that are consistent with the instrumental spectral resolution or are marginally resolved.

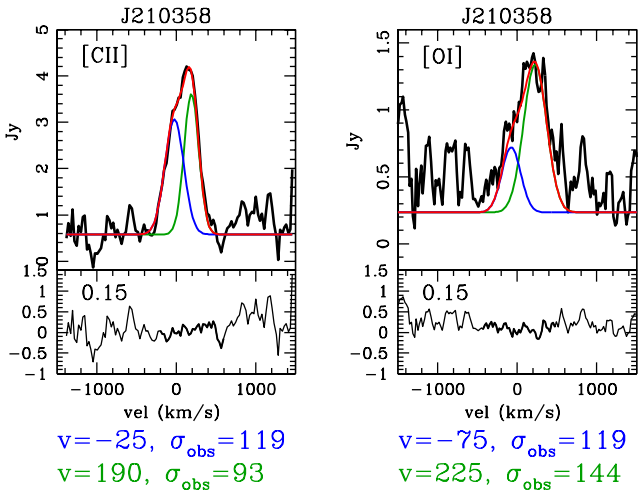

Fig. 3. [CII] and [OI] spectra of SDSSJ210358, with two Gaussian component plus polynomial continuum fit, which yields residuals smaller than a fit with one Gaussian component.

3.2. ^{12}CO(1–0) data

We obtained IRAM PdBI (Guilloteau et al. 1992) observations of four LBAs in the array's compact D configuration between 2005 August and 2007 June. The four targets were selected from the Heckman et al. (2005) sample on the basis of significant detections in 1.2 mm photometry with the Max-Planck Millimeter Bolometer (MAMBO) array on the IRAM 30 m telescope and in at least one IRAS band, on the assumption that dust emission would favor a gas detection experiment. Observations of SDSSJ015028 (five tracks with four or five antennas in operation) and SDSSJ143417 (three tracks with five antennas) were obtained in 2005–06 through program O060; observations of SDSSJ021348 (two tracks with four or five antennas) and SDSSJ210358 (three tracks with four, five, or six antennas) were obtained through program Q073. All observations were calibrated with the CLIC package in the GILDAS environment (Guilloteau et al. 2000), using nearby quasars for gain calibration, bright but more distant quasars for passband calibration, and the radio star MWC349 (or a bright quasar bootstrapped to MWC349) for flux calibration. After modest editing, imaging was done in AIPS (van Moorsel et al. 1996) using moderately robust weighting that yielded synthesized beams of 4.9–7.6 arcsec in diameter. All four sources showed CO(1–0) emission distributions sufficiently compact to allay any concerns about resolved-out flux. Table 6 presents line flux and velocity width measurements derived from integrated spectra of the four galaxies. We also include the data for two additional targets in common with the CARMA sample of Gonçalves et al. (2014). For SDSS015028, observed with both the PdBI and CARMA, we adopt the 50% higher flux from CARMA (which observed the source for longer) but we adopt the width derived from our

Table 6. Line flux and FWHM obtained from single Gaussian plus continuum fit to the PdBI spectra and from Gonçalves et al. (2014).

Name	CO(1–0) Jy km s^{-1}	CO *FWHM* km s^{-1}
015028*	2.37	328.1
021348	1.83 (±0.2)	79.2
080844*	1.74	
092159*	1.04	
143417	1.94 (±0.52)	321.3
210358	10.68 (±0.72)	413.9

Notes. (*) Flux by Gonçalves et al. (2014).

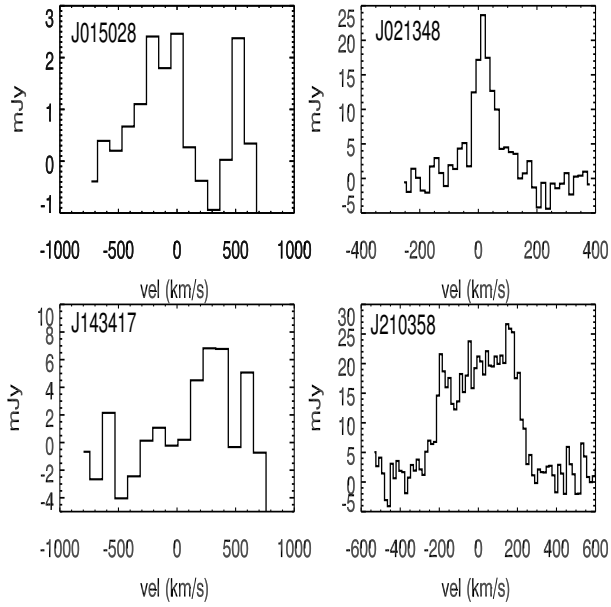

Fig. 4. IRAM PdBI CO(1–0) spectra of four galaxies.

fit, since Gonçalves et al. (2014) did not publish the widths of the lines.

Figure 4 shows the IRAM PdBI CO spectra. The line velocity peaks of [CII] ([OI]) and CO agree well for all galaxies except for SDSSJ143417, where the CO profile peaks at a higher velocity than the [CII] profile. Basu-Zych et al. (2009) describe the kinematics of this galaxy as disturbed, with multiple cores probably arising from a recent merger. It is thus possible that the bulk of the [CII] and CO emission arises from different kinematic components.

4. Analysis

4.1. Comparison of the integrated velocity dispersions of the different gas phases

In this section we compare the velocity dispersion of the atomic, molecular, and ionized gas. Because we do not have spatially resolved velocity dispersion maps of LBAs, and hence we cannot separate rotation from dispersion, we compare the integrated velocity dispersions of the different gas phases.

We obtain the neutral gas global velocity dispersions by correcting the single Gaussian fitted FWHM (Fig. 2 and Table 3) for the instrumental resolution and converting to velocity dispersion. In Fig. 6 we compare these dispersions to those of Hα (from Table 1 of Overzier et al. 2009) and CO, when available. The dispersions of the neutral and molecular emission lines of LBAs agree to within the uncertainties, indicating that the neutral atomic and molecular gas phases in the LBAs share the same kinematics. The Hα velocity dispersions agree with these, to within the uncertainties, for most of the galaxies except for SDSSJ005527 and SDSSJ080844, for which $\sigma_{\mathrm{H}\alpha}$ is almost twice the velocity dispersion of the neutral gas. These are also galaxies with optical tidal emission or companions (see Table 2). It is thus possible that the neutral gas is more concentrated than the ionized gas and does not experience the turbulence of the gas flowing between the interacting galaxies.

The LBA integrated gas velocity dispersions are comparable to those of LBGs (Erb et al. 2006a) and also to the average [CII] intrinsic velocity dispersion (~95 km s^{-1}) of a sample of MS galaxies ($M_* \sim 10^{10}\ M_\odot$) at $0.02 < z < 0.22$ (Ibar et al. 2015). Further, they are significantly lower than the [CII] intrinsic velocity dispersion of a sample of ULIRGs at $z \sim 0.3$ (~220 km s^{-1}) published by Magdis et al. (2014).

4.2. Dust temperatures

To estimate the dust temperatures in our galaxies, we use the method developed by Magnelli et al. (2014; their Sect. 3.1). We fit the FIR photometry (from PACS spectrometer and photometer) of each galaxy with the spectral energy distribution (SED) templates of Dale & Helou (2002, DH). From the best fit to the template, we inferred the dust temperature by using the pairing between dust temperature and DH templates established by Magnelli et al. (2014). Compared to methods relying on direct single modified blackbody (MBB) fits, this technique reduces the bias due to differences in the rest-frame FIR photometric data available for each fit. Nevertheless, because the pairing established by Magnelli et al. (2014) corresponds to a fit of each DH template with a single MBB at $z = 0$, our T_{d} estimates are still in good agreement with other studies in the literature that rely on such single MBB fits. We are thus able to compare our sample with those at high z on the *SFR*-M_* plane, as was done in Magnelli et al. (2014). We list the derived dust temperatures in Col. 1 of Table 7.

4.3. Dust masses and SFR determination

The IR SEDs of our sources were fitted with Draine & Li (2007, DL07) models, using the *Spitzer* photometry at 24 and 70 μm and the *Herschel* photometry at 100 and 160 μm (Fig. 5). These models describe interstellar dust as a mixture of carbonaceous and amorphous silicate grains, whose size distributions are chosen to mimic the observed extinction law in the Milky Way (MW), Large Magellanic Cloud (LMC), or Small Magellanic Cloud (SMC) bar region. In principle, the model includes six free parameters:

- q_{PAH} parameterizes the properties of grains and essentially defines the choice of the dust model;
- U_{min} and U_{max} are the minimum and maximum stellar radiation field to which grains are exposed;
- α is the power of the dust-mass dependence on the radiation field;
- γ is the fraction of dust mass locked into PDRs;
- M_{dust} is the model mass normalization.

The DL07 parameter space has been limited to the range suggested by Draine et al. (2007) for galaxies missing sub-mm data, as in our case. We limit the analysis to MW dust mixtures; $\alpha = 2$; $0.7 \leq U_{\mathrm{min}} \leq 25$ and $U_{\mathrm{max}} = 10^6$. Finally, we use the Li & Draine (2001) values of k_ν. Berta et al. (2016) present a detailed discussion of the use of DL07 models with incomplete

Table 7. Dust temperatures, FIR (40–120 μm) and TIR (8–1000 μm) luminosities, and dust masses derived as described in Sects. 4.1 and 4.2.

Name	$T_{\rm dust}$ K	$L_{\rm FIR}$ $L_\odot$	$L_{\rm TIR}$ $L_\odot$	$M_{\rm dust}$ $10^8 \times M_\odot$	SFR $M_\odot$ yr^{-1}
005527*	49.5 (2.2)	1.10 (0.26)e+11	2.17 (0.10)e+11	0.23 (0.09)	21.99
015028	35.9 (1.0)	2.75 (0.31)e+11	4.02 (0.13)e+11	1.10 (0.12)	40.799
021348	30.2 (1.0)	3.98 (0.61)e+11	5.10 (0.10)e+11	1.45 (0.16)	51.74
080844	49.4 (1.9)	3.71 (0.75)e+10	8.62 (0.73)e+10	4.03 (1.00)	8.75
082001	44.3 (1.0)	8.95 (1.00)e+10	1.60 (0.34)e+11	0.21 (0.01)	16.23
092159	35.9 (1.2)	3.95 (0.69)e+11	5.07 (0.71)e+11	1.80 (0.41)	51.44
093813	39.6 (2.8)	3.40 (1.30)e+10	6.08 (0.25)e+10	0.14 (0.32)	6.17
143417	29.3 (1.0)	7.70 (1.40)e+10	1.08 (0.49)e+11	0.79 (0.27)	11.01
210358	33.4 (1.0)	2.54 (0.40)e+11	5.11 (0.12)e+11	7.2 (1.10)	51.90

Notes. Star-formation rates are derived from $L_{\rm TIR}$ using the scaling relation given by Kennicutt & Evans (2012), divided by a factor of 1.7 to convert from the Salpeter to the Chabrier IMF that we adopt in this work.

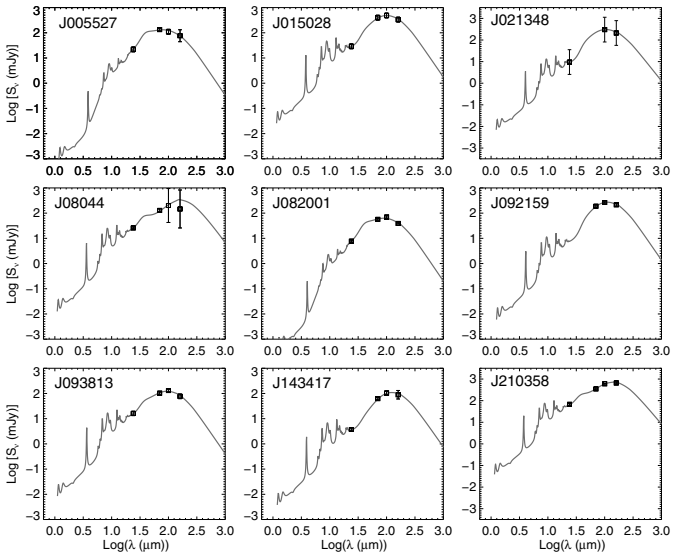

Fig. 5. SED fits of LBAs FIR photometry using the method explained in Sect. 4.3.

SEDs and a thorough discussion of the uncertainties and possible systematics in the determination of $M_{\rm dust}$.

From each fit to an SED we also calculate $L_{\rm IR}$(8–1000 μm), and from this we calculate the SFR following the prescription in Kennicutt & Evans (2012); we divided by the factor 1.7 to convert from the Salpeter IMF to the Chabrier IMF that we assume in this work in order to be consistent with SFR estimates for some high-z galaxy samples. We list in Table 7 $L_{\rm IR}$ and $M_{\rm dust}$ (with 1σ uncertainties) and SFR. The SFRs derived in this work are a factor of 2 smaller than those given by Overzier et al. (2009) and listed in Table 1, which are calculated from Hα and the 24 μm flux. However, the SFRs derived from the IR (8−1000 μm) luminosities given in Overzier et al. (2011) are in much better agreement (within ∼20%) with ours, and the discrepancy can be ascribed to the different methods used to derive the IR luminosities.

5. Results

5.1. Why study the neutral atomic gas in galaxies?

Until recently, the ISM of high-redshift galaxies has been principally probed via their ionized (Glazebrook 2013, and references therein) and molecular gas (Tacconi et al. 2013; Carilli & Walter 2013). In particular, the molecular gas fraction and its depletion timescale are two fundamental parameters in determining galaxy evolution (Tacconi et al. 2010; Daddi et al. 2010b). However, the neutral atomic medium is another important component of a galaxy's ISM, and the study of its evolution over cosmic time is complementary to that of the ionized and molecular gas.

The bulk of the atomic medium is traced by the 21 cm HI line emission, which unfortunately is not yet generally accessible at redshift ≳0.2. The [CII] and [OI] lines are the main cooling lines of the cold neutral medium (CNM; $n > 10$ cm^{-3} and $T <$ few $\times$ 10^2 K), and therefore they can also be used to trace the neutral atomic phase. With the advent of (sub)mm interferometers, this is now possible up to very high z (∼6−7).

The CNM is mostly concentrated at the interfaces between HII regions and their parent molecular clouds (photo-dissociated regions or PDRs). This means that [CII] and [OI] emission are related to star formation and can be used as SFR tracers. This connection in particular has attracted much interest in recent years because the detection of the [CII] line in high-redshift galaxies could potentially be used to derive their SFRs. However, the two local [CII] – SFR calibration relationships (De Looze et al. 2014; Herrera-Camus et al. 2015) have high intrinsic dispersion (0.3 dex), and the FIR continuum is usually detectable in less time than the [CII] line. Moreover, there is growing evidence that the [CII]-SFR relationship followed by very high-redshift galaxies is different from the local relationship. SFGs at $z > 5$ usually have less [CII] emission for a given SFR (i.e., they have a low [CII]/IR ratio) than local SFGs (Pentericci et al. 2016, and references therein). Therefore, it is not clear whether the [CII] emission is a better SFR tracer than the FIR continuum.

On the other hand, the study of the content and the dynamical state of the neutral gas that can be obtained with observations of lines gives complementary information on the more general state of the ISM in galaxies, its interplay with the heating sources and its evolution over time.

In recent years, many authors have shown that normal star-forming galaxies (SFGs) from $z = 0$ to $z \sim 3$ lie on the Kennicutt-Schmidt relation (Genzel et al. 2010; Tacconi et al. 2010, 2013; Daddi et al. 2010a; Combes et al. 2013), while only mergers, that is, local ULIRGs and submillimeter galaxies (SMGs) at $z = 2$−3, depart from this relation. However, the ISM conditions in local and high-redshift SFGs differ in several ways, with high-redshift galaxies showing not only higher

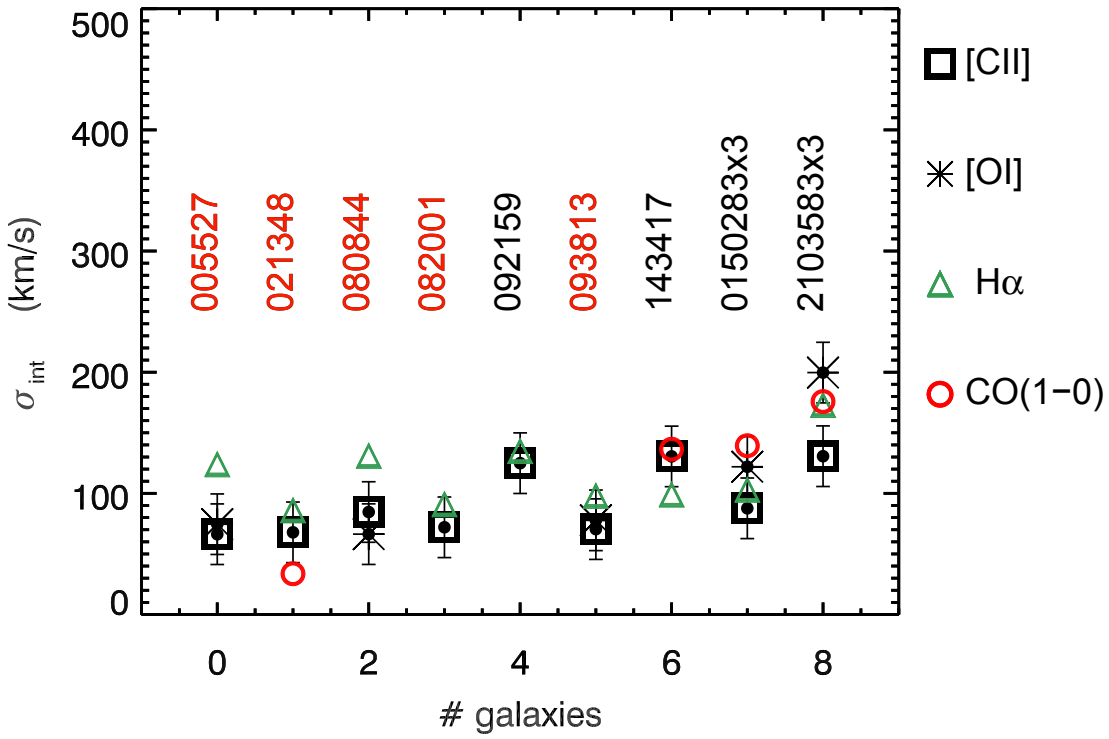

Fig. 6. Comparison of the intrinsic global velocity dispersions obtained from the PACS [CII] and [OI] lines, with those of CO presented in this work and Hα presented in Overzier et al. (2009). Galaxies marked in red are not spectroscopically resolved.

pressure and column density but also higher intrinsic velocity dispersion of the ionized medium (30–90 km s^{-1}) than local SFGs (~5–10 km s^{-1}) (Law et al. 2007; Förster Schreiber et al. 2009; Cresci et al. 2009; Tacconi et al. 2010; Wisnioski et al. 2015). High velocity dispersion suggests the existence of large amounts of turbulence most likely due to star formation feedback (Newman et al. 2012a). Moreover, these systems often host very large (~1 kpc) clumps that could be as massive as a few 10^9 $M_\odot$ (Elmegreen et al. 2008; Genzel et al. 2011; Swinbank et al. 2012; Freundlich et al. 2013) and be sites of powerful outflows (Newman et al. 2012b). The emission from these clumps is compatible with photoionization by star formation and shocks from the outflowing material. These characteristics could influence the [CII] emission in high SFGs in a different way than what is observed in local SFGs.

In what follows, we analyze the [CII] (and [OI]) content of LBAs in order to establish a reference for planning similar observations of high-redshift galaxies. So far, the observations of [CII] in high-redshift galaxies, even if steadily increasing in number, have mostly targeted very luminous galaxies (e.g., QSOs, SMGs) and only in the last few years have the first attempts to observe this line in normal SFGs at high z started to yield the first clear detections (Maiolino et al. 2015). This work aims at characterizing the conditions in the CNM, and how it scales with other fundamental properties of LBAs in order to provide nearby analogs for ISM studies of high-redshift star-forming galaxies.

5.2. Physical conditions in the neutral atomic gas in LBAs

In PDRs, atomic gas cooling occurs mainly through the [CII] and [OI] lines while the heating is due to the photoelectric effect on dust grains. Thus, the ratio between the total emission from the FIR fine structure lines and the total infrared emission from grains gives the total photoelectric yield. By comparing the observed ratio with that predicted by a model, one can derive fundamental physical parameters of the neutral ISM associated with the PDRs. In the five galaxies observed in both [OI] and [CII], we can rule out shocks as the major emission mechanism, because the [OI]/[CII] ratio is much smaller than what is expected for shocks (~10; Hollenbach & McKee 1989), and is very similar to what is expected in normal PDRs. We therefore proceed to model the neutral gas FIR fine structure lines and the continuum as arising in PDRs.

We adopt the model of Kaufman et al. (1999), which considers a one-dimensional semi-infinite slab illuminated from one side that produces optically thin [CII], IR ($\gtrsim$30 μm) and optically thick [OI], such that only one side of the cloud emits [OI] at 63 μm. The PACS beam encompasses many clouds, which is equivalent to considering many clouds randomly illuminated. Thus, we reduce the [OI] emission predicted by the model by a factor of 2. We also integrate the IR flux under the IR SED produced as described in Sect. 4.2. We note that we do not attempt to correct the total [CII] emission for the contribution from ionized gas. This is usually done by scaling from the [NII] line at 122 μm or, even better, from the lower energy [NII] line at 205 μm. Measurements of these lines are not available for LBAs. Thus, the observed [CII] is an upper limit to the [CII] arising in the neutral atomic medium.

We plot in Fig. 7 the density of the neutral medium $n_{\rm H}$ and the far-UV (FUV) interstellar radiation field (ISRF) expressed in G_0 units[3] obtained for LBAs. We also show the results obtained by applying the same PDR models to the same set of lines and total IR emission observed in five other galaxy samples: (1) a local sample of galaxies assembled from the PACS Guaranteed Time Program SHINING (P.I., E. Sturm), published in part by Graciá Carpio et al. (2011), and in Herrera–Camus et al., in prep., which includes HII galaxies, Seyfert 1 and 2 galaxies, LINERs, LIRGs, ULIRGs and QSOs; (2) the central regions of

[3] G_0 is the FUV (6–13.6 eV) ISRF normalized to the solar neighborhood value expressed in Habing flux: 1.6×10^{-3} erg s^{-1} cm^{-2}.

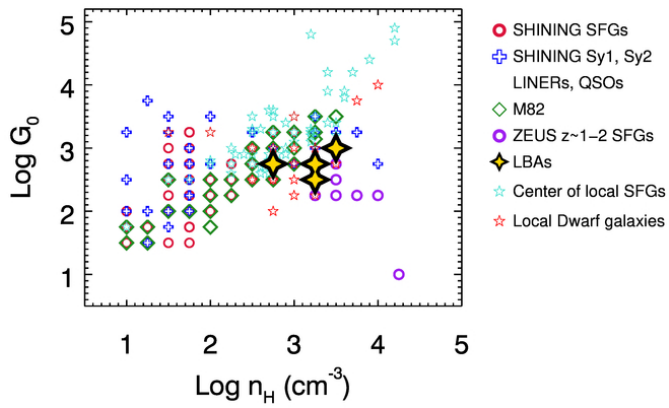

Fig. 7. LBAs on the ISRF (expressed in G_0 units) – atomic gas density $n_{\rm H}$ plane as inferred from the PDR modeling (following Kaufman et al. 1999). We also plot the results of the same modeling for the subsample of SHINING galaxies that have [OI],[CII], and FIR observations (Graciá Carpio et al. 2011; Herrera-Camus et al., in prep.), some resolved regions inside M82 (Contursi et al. 2013), the central regions of local SFGs observed with ISO-LWS (Malhotra et al. 2001; Negishi et al. 2001), the sample of local dwarfs from Cormier et al. (2015), and a sample of $z \sim 1-2$ SFGs observed with ZEUS (Brisbin et al. 2015).

local star-forming, starburst, and (a few) AGN dominated galaxies observed with ISO-LWS published by Malhotra et al. (2001) and Negishi et al. (2001); (3) a sample of local low-metallicity dwarf irregulars observed with PACS presented in Cormier et al. (2015); (4) some resolved regions in the disk and the outflow of M82 (Contursi et al. 2013); and (5) a sample of star-forming galaxies at $z \sim 1-2$ observed with the ZEUS instrument at CSO and with *Herschel*, published by Brisbin et al. (2015). The latter have higher stellar masses and SFRs than our targets, but they constitute the only available high-redshift sample of SFGs observed in [CII], [OI], and FIR continuum for which it is possible to apply the same PDR modeling as we have used for the LBAs.

We stress that, for the comparison samples, we do not use the published $n_{\rm H}$ and G_0 values, but we model the TIR continuum and the FIR fine structure line emission again, in the same way and by applying the same correction factors as for the LBA sample. This ensures a safe comparison amongst the different samples.

We find $10^{2.8} < n_{\rm H} < 10^{3.5}$ and $10^{2.5} < G_0 < 10^{3.0}$ in LBAs, placing them on the high density-high G_0 part of the correlation, and comparable to the physical conditions in starbursts. This is consistent with the starburst nature of most of the original LBA sample as shown by Overzier et al. (2008, 2009). On the other hand, the range of $G_0/n_{\rm H}$ ratios obtained for the LBAs, most of the dwarfs and the ZEUS galaxies is lower than the main relationship followed by the other galaxies. This could be due to a lower G_0 and/or a higher $n_{\rm H}$. Applying a 0.8 correction factor to the PDR [CII] fluxes to account for contributions from ionized gas (e.g., Malhotra et al. 2001) has negligible effect on the resulting G_0 and $n_{\rm H}$ parameters. Brisbin et al. (2015) attribute this difference to a moderately low G_0 value due to the large, several kpc extent of star formation in their sample. This could also explain the low G_0 values of LBAs, since their UV extent is ~5″ (~5 kpc; Gonçalves et al. 2010; we also refer to additional evidence discussed in Sect. 6.2). On the other hand, we cannot rule out higher gas density as a contributing factor to the low $G_0/n_{\rm H}$ values in LBAs and high-z galaxies in comparison to local galaxies.

Figure 8 shows the histogram of thermal pressures and gas surface temperatures obtained from our modeling. We separate the local SFGs and starbursts (shown in gray) from the local LINERs, Seyfert 1 and 2 galaxies present in the SHINING, Malhotra et al. and Negishi et al. samples (pink), and the low metallicity dwarf sample (green). For the LBA and ZEUS samples, we indicate the ranges covered by these parameters, since the number of galaxies in each sample is small.

LBAs and the high-z galaxies of Brisbin et al. (2015) have pressures and temperatures that are on the high and low sides of the histogram ranges, respectively. The distribution of the pressures of local SFGs and starbursts shows a bimodality not present in the temperature distribution, with the high-pressure second peak dominated by starbursts. This second peak overlaps with the values found in dwarfs and corresponds to the range spanned by LBAs and high-z SFGs. The thermal pressures of the cold neutral medium derived for LBAs are within the range of thermal pressures derived by Overzier et al. (2009) from the ionized gas for the whole LBA sample. These pressures are much higher than the mean thermal pressure of the CNM in our galaxy (~3800 K cm^{-3}), and of atomic dominated regions in nearby galaxies (Jankins & Tipps 2011; Herrera-Camus et al. 2017), and higher than those derived in the nuclei of the Antennae from X-ray observations (Fabbiano et al. 2003). By assuming that thermal pressure is about 10% of the total hydrostatic pressure (Cox 2005), we derive a total pressure of about 5×10^6 K cm^{-3} that is in the range of the total hydrostatic pressure at mid plane measured in high-z main sequence galaxies ($0.3-10 \times 10^7$ K cm^{-3}, Swinbank et al. 2011; Genzel et al. 2010).

We conclude that the physical conditions of the neutral atomic gas in LBAs are quite extreme with respect to the mean properties of the local sample of star-forming galaxies, exhibiting lower atomic gas temperatures, higher pressure, and likely higher densities, as found in low-metallicity dwarfs and starbursts. These same conditions are also seen in the small sample of high-z star-forming galaxies observed to date.

We note that hosting a DCO does not necessarily imply the most extreme ISM conditions. In fact, the only galaxy hosting a DCO observed in both [CII] and [OI], for which PDR modeling is possible (SDSSJ08044), has among the lowest values of P, G_0, and $n_{\rm H}$, and the highest $G_0/n_{\rm H}$ ratio and T. DCOs are very similar to the massive clumps detected in high-z star-forming galaxies (Newman et al. 2012b) and therefore one would expect that their presence would be related to more extreme ISM conditions. Unfortunately, with our limited number of objects, it is difficult to draw conclusions about a potential connection between the conditions of the ISM and the presence of a DCO, by analogy with the clumps observed in high-z SFG disks.

5.3. The correlation of [CII] with other ISM tracers

In this Section we present and discuss correlations between the [CII] emission, the infrared dust emission, and the molecular gas emission of LBAs and compare them to those found in other galaxy samples at low and high redshifts.

We first present the diagnostic plot that relates the [CII]/FIR ratio with the FIR luminosity (upper left panel of Fig. 9). We include in this figure the values for the LBA sample, the SHINING sample, a sample of low-redshift QSOs published by Zhao et al. (2016), a sample of intermediate-z ($z \sim 0.2$) ULIRGs published by Magdis et al. (2014), and a sample of high-z sources collected by Carilli & Walter (2013) with recent updates (we refer to the figure caption for details). The high-z sample includes relatively recent high- and very-high-redshift

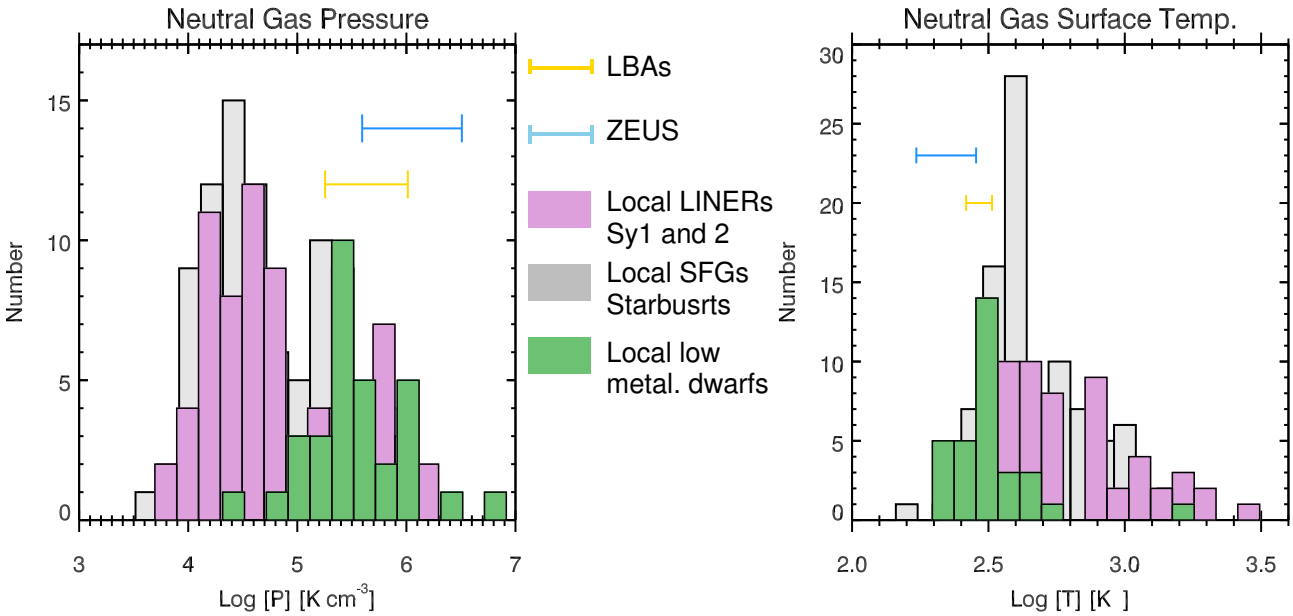

Fig. 8. Histogram of the atomic neutral gas thermal pressures and surface temperatures obtained by applying the PDR modeling to the galaxies belonging to different galaxy samples. The local SFGs and starbursts belonging to the SHINING sample, and the samples from Malhotra et al. (2001) and Negishi et al. (2001) are shown in gray; the subsample of galaxies classified as LINERs, Sy1 and Sy2, are shown in pink; and the low-metallicity dwarf galaxies from Cormier et al. (2015) are shown in green. The ranges of ISM parameters obtained by modeling the LBAs and the ZEUS samples at $z \sim 1-2$ are shown in yellow and light blue, respectively.

[CII] detections, which have become more numerous thanks to new very sensitive interferometers. However, these objects are still biased towards very luminous ($L_{\rm FIR} > 10^{12}\ L_\odot$) galaxies (typically QSOs and SMGs) even when the targets are lensed systems. Nevertheless, these recent observations of high-z systems shed new light on the [CII]-FIR relation, vastly expanding its characterization in comparison with what was known only a decade ago when the diagram was limited to very nearby ($z < 0.1$) systems. Figure 9 shows that the [CII]/FIR ratio of local systems decreases with FIR luminosity (Malhotra et al. 2001; Luhman et al. 2003), with a knee at $L_{\rm FIR} > 10^{11}-10^{11.5}\ L_\odot$ beyond which the decline becomes even steeper. Extrapolating this behavior, we might expect galaxies with $L_{\rm FIR} > 10^{12}\ L_\odot$ to have low [CII]/FIR ratios. Observations of high-z very IR-luminous galaxies show that this is not the case; many high-z very FIR-bright sources show [CII]/FIR ratios comparable to those of local, less luminous galaxies. This was first shown by (Maiolino et al. 2009; Hailey-Dunsheath et al. 2010; Stacey et al. 2010) and confirmed later by many other authors (Maiolino et al. 2012; Wagg et al. 2012; Gallerani et al. 2012; Venemans et al. 2012, and reference therein). The high-z galaxies tend to lie in a sequence parallel to that observed at low redshift, shifted to higher FIR luminosities. In this sequence, the objects with confirmed AGNs tend to have lower [CII]/FIR ratios than those without AGN contributions (Hailey-Dunsheath et al. 2010). Thus, at high z there are galaxies with luminosities as high as or higher than those of local ultraluminous galaxies, but with "normal" [CII]/FIR ratios.

LBAs follow a correlation similar to that of the low-luminosity systems, exhibiting a range in [CII]/FIR ratio decreasing with $L_{\rm FIR}$ that however never reaches the range of [CII]-deficient galaxies. LBAs are not [CII]-deficient, and it is likely that $z \sim 2$ star-forming galaxies also have normal [CII]/FIR ratios, enhancing the likelihood that we can study their [CII] properties with ALMA (Sect. 6.4).

The upper right panel of Fig. 9 shows the [CII]/FIR ratio as a function of CO/FIR ratio and the $n_{\rm H}$ and G_0 grids of the Kaufman et al. model. With the exception of SDSSJ015028, which has a particularity low CO/FIR ratio, LBAs overlap the local SFGs but lie in ranges of $n_{\rm H}$ and G_0 higher than what we obtain by modeling the [CII] and [OI] lines. This is likely due to the fact that we are using a different pair of lines and that the Kaufman et al. model requires as input the total IR luminosity and not the FIR luminosity used in this diagnostic.

In the lower left panel of Fig. 9, we show the [CII]/FIR ratio as a function of the $L_{\rm FIR}/M_{\rm H_2}$ ratio for galaxies with [CII] and CO(1-0) data (the latter used to estimate H_2 masses) available. This diagram was first shown by Graciá Carpio et al. (2011). The values of $L_{\rm FIR}/M_{\rm H_2}$ for LBAs have been obtained using a Milky Way conversion factor to derive $M_{\rm H_2}$ from the CO luminosity ($\alpha_{\rm CO} = 4.3\ M_\odot$ (K (km s^{-1} pc^2)$^{-1}$). If we use a ULIRG conversion factor ($\alpha_{\rm CO} = 0.8\ M_\odot$ (K (km s^{-1} pc^2)$^{-1}$, Downes & Solomon 1998), the derived H_2 masses would be smaller and the $L_{\rm FIR}/M_{\rm H_2}$ ratio larger, such that for some galaxies it would exceed the threshold of the high-efficiency SF mode. However, as we discuss in Sect. 6.1, our analysis favors the Milky Way conversion factor for LBAs. We note that of the four LBAs with DCOs, only SDSS021348 falls below the tight correlation, although this is not the case if a ULIRG CO-H_2 conversion factor is used.

The dichotomy between very luminous and less luminous systems shown before is less evident when the [CII]/FIR ratio is plotted as a function of $L_{\rm FIR}/M_{\rm H_2}$. In galaxies in which $L_{\rm FIR}$ is predominantly powered by star formation, the $L_{\rm FIR}/M_{\rm H_2}$ ratio is, to first approximation, the ratio between the energy released by the star formation and the gas reservoir from which the stars form, and therefore is a parameter directly related to the star-formation efficiency (González-Alfonso et al. 2008, 2015; Graciá Carpio et al. 2011). On this diagram, low- and high-redshift galaxies follow the same correlation. This suggests that

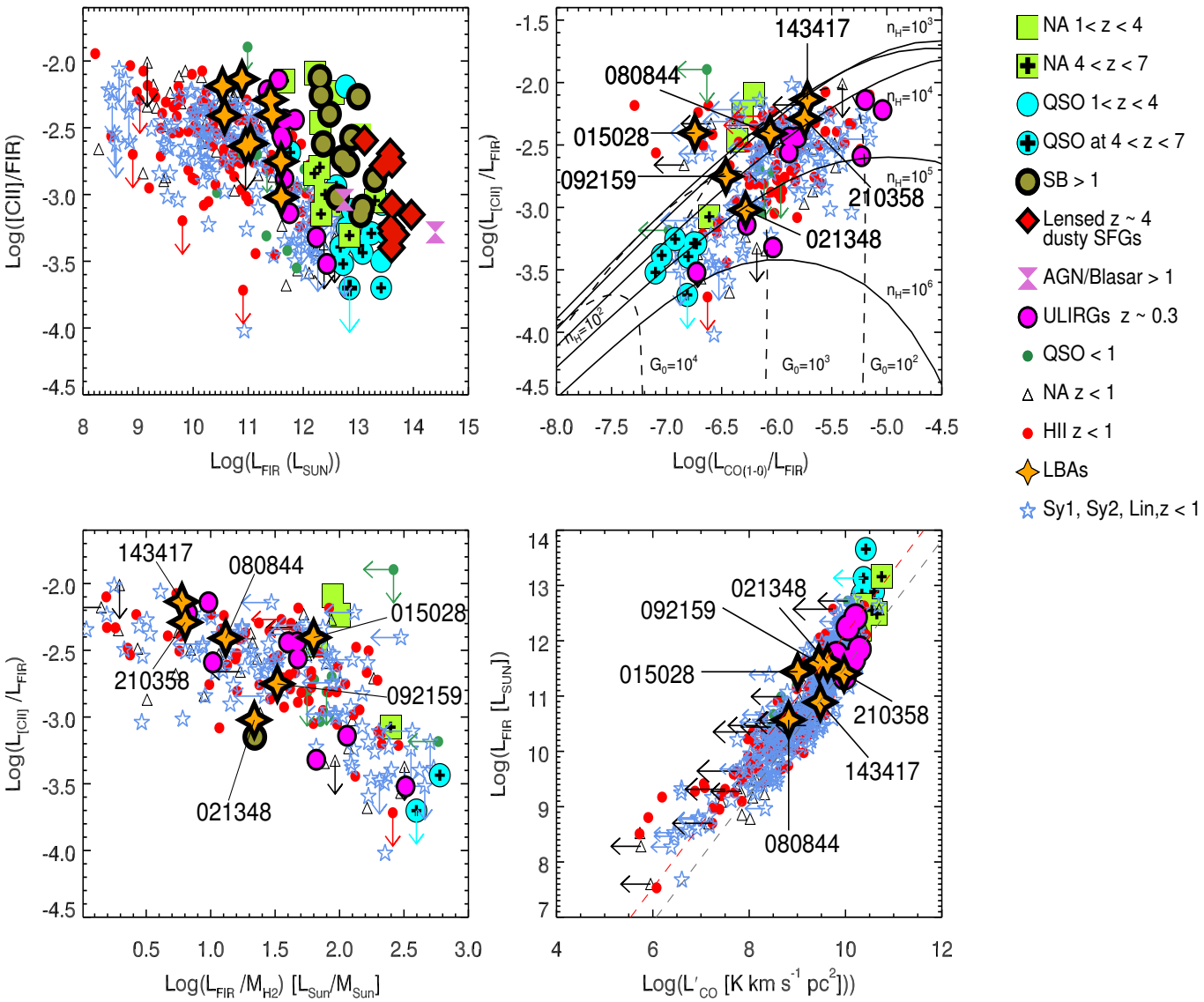

Fig. 9. *Upper left panel*: [CII]/FIR ratio (defined as in Helou et al. 1988) as a function of FIR luminosity for the LBA sample, a set of local galaxies belonging to the SHINING sample, and data collected in the literature (Herrera-Camus et al., in prep.; Zhao et al. 2016). High-redshift galaxies are taken from Carilli & Walter (2013) supplemented by data from Wang et al. (2013), De Breuck et al. (2014), Schaerer et al. (2015), Bañados et al. (2015), Yun et al. (2015), and Bothwell et al. (2017). The sample of ULIRGs at $z \sim 0.3$ is from Magdis et al. (2014). *Upper right panel*: [CII]/FIR ratio as a function of CO(1–0)/FIR ratio for all galaxies included in the previous panel with available CO data. We also plot the PDR model grid for constant G_0 and $n_{\rm H}$ from Kaufman et al. (1999). *Lower left panel*: [CII]/FIR ratio as a function of $L_{\rm FIR}/M_{\rm H_2}$ ratio for the galaxies with available CO(1–0) observations. *Lower right panel*: FIR luminosity as a function of CO luminosity. We also plot the relationships followed by local and high-redshift star-forming galaxies (gray dashed line) and by local ULIRGs and distant SMGs (red dashed line), from Genzel et al. (2010).

the physical mechanism responsible for the different [CII] emission regimes is the same locally and in the distant Universe.

Graciá Carpio et al. (2011) find that the far-infrared fine-structure line deficit (relative to the FIR) increases as the star-formation efficiency ($L_{\rm FIR}/M_{\rm H_2}$) rises. They attribute this to higher ionization parameters, resulting in the absorption of a higher fraction of the available UV photons by dust, leaving fewer photons to ionize and heat the gas (Luhman et al. 2003; Abel et al. 2009; Fischer et al. 2014; Goicoechea et al. 2015). Graciá Carpio et al. (2011) and Díaz-Santos et al. (2013) show that galaxies with a [CII]/FIR deficit lie above the MS. Thus, LBAs, that are above the local MS in Fig. 1, nevertheless have a [CII]/FIR ratio typical of MS galaxies. We discuss this point further in Sect. 6.2. The lower left panel of Fig. 9 shows that the LBAs for which we have CO data occupy the relatively high-[CII]/FIR region of the diagram with $L_{\rm FIR}/M_{\rm H_2}$ ratio lower than the threshold found by Graciá Carpio et al. (2011), ~80 $L_{\rm FIR}/M_{\rm H_2}$. This is not what one might have expected in regions of high sSFR, such as the clumps in DCOs.

The last relationship that we analyze is between $L'_{\rm CO}$ and FIR luminosity (lower right panel of Fig. 9), in which we also show, plotted with red and gray dashed lines, the scaling relations for mergers and the star-forming galaxies that Genzel et al. (2010) obtain by fitting data for local and high redshift ($z \sim 2$) galaxies. Most of the six LBAs for which we have CO data are consistent with typical MS SFEs. The only exceptions are SDSSJ015028 and SDSSJ021348 (a DCO), which lie on the merger sequence: for a given amount of molecular gas, they

have FIR emission and hence SFR much higher than that of a star-forming galaxy. SDSSJ14347 and SDSSJ015028 are probably interacting systems based on a kinematic integral field spectroscopic study of their ionized gas by Gonçalves et al. (2010), but only the latter shows the "high"-efficiency mode of star formation typical of merging systems. We note that the PACS beam is large enough to include both interacting components. On the contrary, SDSSJ021348, which contains a DCO, is on the merger sequence even though no clear signs of merging or interactions have been detected in the ionized gas or the UV light distribution.

We conclude that most LBAs exhibit an efficiency in turning gas into stars similar to that of MS galaxies, despite the fact that they are starbusts and lie above the local MS.

Finally, we have investigated if the [CII]/FIR and LIR/CO ratios depend on galaxy morphology, that is, whether galaxies are isolated or in some stage of interaction/merging (see Table 1). There is a tendency for the three isolated galaxies to have lower ratios than the others, although the small sample size prevents us from making a strong statement.

5.4. [CII] and [OI] as SFR tracers

In this section we explore the locations of LBAs in the SFR – [CII] and [OI] planes and we compare them to observed relationships at low and high redshifts. The two most recent works on the local SFR-[CII] ([OI]) relationship are those of De Looze et al. (2014) and Herrera-Camus et al. (2015). De Looze and coauthors explore these relations for a wide sample of local galaxies spanning several magnitudes in metallicity, and for a large variety of galaxy types, including dwarfs, low-metallicity galaxies, HII/starbursts, composite and AGNs, ULIRGs as well ad some high-z very-IR-luminous sources. They use SFRs derived from the *GALEX* FUV plus *Spitzer*–MIPS at 24 μm for the dwarf galaxy sample and SFRs derived from $L_{\rm IR}$ for the other galaxy populations, all assuming a Kroupa IMF (Kroupa & Weidner 2003).

Figure 10 shows these relationships for the [CII] and the [OI] lines. On the left panel, the locations of the LBAs are plotted together with those of two galaxy samples at comparable redshift: A sample of MS galaxies ($M_* \sim 10^{10}$ $M_\odot$) at redshift $0.02 < z < 0.2$ from Ibar et al. (2015)[4], and the $z \sim 0.3$ ULIRG sample of Magdis et al. (2014). We plot, with different colors, galaxies classified as composite/AGN and HII on the BPT diagram. In order to be consistent with the derivation of the De Looze et al. relationships, we have calculated the SFRs of all galaxies from $L_{\rm IR}$ using a Kroupa IMF, following the prescription from Table 3 of Kennicutt & Evans (2012).

Figure 10 shows that LBAs are well below the relationship followed by ULIRGs (green lines), which in general have a significant [CII]-deficit. But it also shows that there is a high spread in the values of all samples, and that galaxy locations are not always consistent with their BPT classifications. Most LBAs are above the relationship followed by local dwarfs. The two LBAs with lower SFRs closer to the dwarf relationship, SDSSJ093813 and SDSSJ080844, have the lowest and the highest metallicity of the sample, respectively (Table 1).

Herrera-Camus et al. (2015) explore the SFR–[CII] relation for the KINGFISH sample of local star-forming galaxies, both within each galaxy and globally. They emphasize that it is better to use the relation between the surface brightnesses of SFR and [CII] rather than the luminosities. Since LBAs are point sources for the PACS beams, we cannot use this approach. Instead, we use their Eq. (3) relating SFR and [CII] luminosities. This relation is shown as a dashed black line in Fig. 10 after correction of SFR values from the Salpeter to the Kroupa IMF. This relation is lower by a factor of ~4 in SFR with respect to that derived by De Looze et al. for HII/starburst galaxies. This is probably due to a higher percentage of starburst systems in the HII/starburst sample of De Looze et al. relative to the more normal star-forming galaxies in the KINGFISH sample (we refer to Fig. 10 in Herrera-Camus et al. 2015). The relation falls too low to match most LBAs and most memebrs of the other two galaxy samples.

The green box in Fig. 10 represents the location of MS star-forming galaxies with stellar masses between $\sim 10^9 - 10^{10}$ $M_\odot$ at $z \sim 7$ from Pentericci et al. (2016). They show that for a given SFR, the [CII] emission is lower than what is predicted by the local SFG relationship. This is not the case for LBAs, which although with high dispersion, are closer to the local starburst relationship. We conclude that in LBAs and in SFGs at $z \sim 1-2$, [CII] can be used as a rough SFR estimator. However, the fact that FIR continuum emission is detectable in less time than the FIR fine structure lines makes the use of [CII] as a SFR tracer less attractive.

5.5. Summary of main results

In this section we present the following results. (1) LBAs do not show a [CII] line deficit relative to $L_{\rm IR}$ or $L_{\rm FIR}/M_{\rm H_2}$. (2) The physical conditions in their neutral atomic gas are different from those of local SFGs, and more similar to those found in local starbursts, low-metallicity dwarfs, and high-z galaxies in terms of thermal pressure, temperature, and $G_0/n_{\rm H}$ ratio. There is some evidence that this difference is independent of the presence of a DCO. (3) LBAs do not overlap with starbursts in the density-FUV ISRF diagram, but rather with local low-metallicity dwarfs and with $z \sim 2$ SFGs observed with ZEUS at CSO. (4) Most LBAs have SFEs similar to those of MS galaxies, despite their high sSFRs. (5) LBAs roughly follow the local HII/Starburst SFR-[CII] relationships. This means that the [CII] emission in LBAs and in similar galaxies at high redshift can be used to estimate their SFRs, although with uncertainties of the order of a factor of 2–3.

6. Discussion: the neutral ISM properties of LBAs in the context of galaxy evolution

6.1. Total molecular gas fraction

In recent years, many authors have shown that the molecular gas fraction of star-forming galaxies in a given stellar mass range, defined as the ratio of the total H_2 mass to the sum of the stellar plus molecular gas mass, increases from 0.08 to 0.47 as the redshift increases (Tacconi et al. 2013), with a possible flattening at higher redshifts (Saintonge et al. 2013; Magdis et al. 2012a), although the flattening is not yet confirmed Béthermin et al. (2015). The question we address in this section is whether or not our targets have a high gas fraction, strengthening also in this respect their analogy with SFGs at $z \sim 2$.

Using different methods, we have calculated the total molecular gas fraction for LBAs for which we have CO(1–0) data. We estimate the H_2 mass with three different CO-H_2 conversion factors: One used for ULIRGs ($\alpha_{\rm CO} = 0.8$ $M_\odot$ pc^{-2} (K km s^{-1})$^{-1}$), one for the Milky Way ($\alpha_{\rm CO} = 4.3$ $M_\odot$ pc^{-2} (K km s^{-1})$^{-1}$), and

[4] From the original sample of Ibar et al. (2015), we have excluded the galaxies classified as elliptical and elliptical irregular.

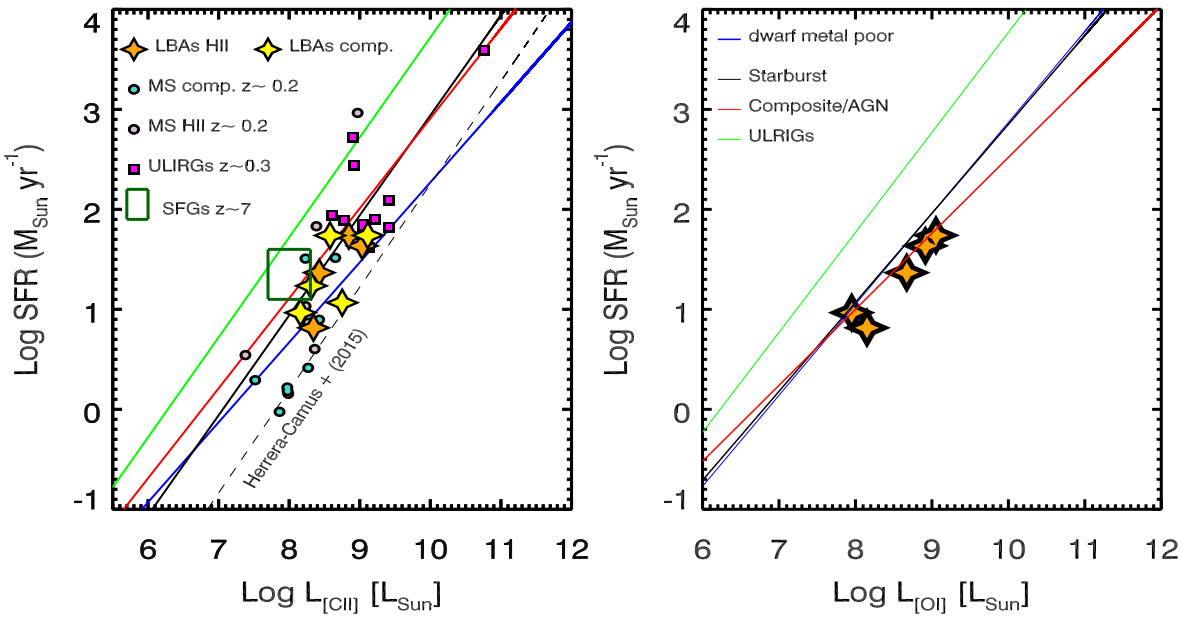

Fig. 10. Relationship of SFR with [CII] (*left panel*) and [OI] (*right panel*) luminosity of LBAs. In the *left panel* we add samples of massive MS ($M_* \sim 10^{10}\ M_\odot$) galaxies at $z \sim 0.3$ from Ibar et al. (2015) and of ULIRGs at $z \sim 0.2$ from Magdis et al. (2014). In the LBA and the Ibar et al. samples, we assign different colors according to galaxy BPT classifications. The green box indicates the position of four MS SFGs at redshift 7 published by Pentericci et al. (2016). The lines indicate the relationships found by De Looze et al. (2014) for samples of different types of local galaxies (solid colored lines, as shown in the legend) and the relation followed by a sample of normal local spirals presented in Herrera-Camus et al. (2015; dashed black line). The SFRs of all galaxies have been derived from $L_{\rm IR}$ and a Kroupa IMF to be consistent with the derivation of De Looze et al. (2014).

one depending on gas metallicity Z as given by Genzel et al. (2012): $\log(\alpha_{\rm CO}) = -1.27 \times Z + 1.18$. We also calculate the H_2 masses from the dust masses listed in Table 7, by using a dust to gas mass ratio formula varying with metallicity given by Genzel et al. (2015)[5]. This formula calculates the dust to molecular gas ratio by assuming that in the galaxies, the molecular gas dominates the atomic phase. The column density value for the atomic to molecular gas transition is $\Sigma_{\rm trans} \sim 14\ M_\odot\ {\rm pc}^{-2}$ (Bigiel & Blitz 2012). We can derive the average $\Sigma_{\rm HI}$ for three LBAs (SDSS0150283, SDSS093813, and SDSS2103583) for which we have PDR model results and FIR sizes from Lutz et al. (2016). We calculate the mass of the atomic hydrogen associated with the [CII] and [OI] emission by applying:

$$\frac{M_{\rm [CII]}({\rm H})}{M_\odot} = 1.34 \times \left(\frac{L_{\rm [CII]}}{L_\odot}\right) \times \left(\frac{1 + 2e^{(-92/T)} + n_{\rm crit}/n_{\rm H}}{2e^{(-92/T)}}\right), \qquad (1)$$

(see Janssen et al. 2016, for details), where we have linearly scaled the $\chi_{\rm C^+}$ abundance by the ratio between the solar metallicity assumed by Pettini & Pagel (2004; $Z_\odot = 8.66$) and the metallicity listed in Table 1. We obtain $\Sigma_{\rm HI}$ equal to 113, 15, and 159 $M_\odot\ {\rm pc}^{-2}$, respectively, close or above the transition threshold. Hence, we can safely assume that the dominant gas phase in LBAs is molecular and derive gas masses from dust masses.

We find an average gas fraction similar to that of local SFGs $\langle f_{\rm gas}\rangle = 0.08$ only when using the ULIRG conversion factor. In all the other cases, the derived gas fractions are $\langle f_{\rm gas}\rangle = (0.3{-}0.4{-}0.5)$ depending on the adopted conversion, that is, close to the typical gas fraction found in high-redshift galaxies (Tacconi et al. 2013). Gonçalves et al. (2014) have presented CO(1–0) data for another sample of LBAs with which we have four galaxies in common, and they reach similar conclusions.

6.2. LBAs and the main sequence

As already mentioned in Sect. 2.1 and shown in Fig. 1, LBAs lie above the main sequence at $z = 0$. In this section we address the following question: do LBAs have the typical ISM properties of local galaxies above the main sequence, or do they behave as typical high-redshift main sequence galaxies? In order to answer this question, we analyze quantities tracing different LBA ISM properties as a function of distance from the main sequence at $z = 0$, 1, and 2 and we compare the LBAs to other galaxy samples at low and high redshifts.

To be consistent with our derivation of SFRs and dust temperatures, we show the distances calculated with respect to the MS defined in Magnelli et al. (2014) and listed in Col. 3 of Table 8. Table 8 also lists the distances from other MS definitions, namely those derived in Speagle et al. (2014) Whitaker et al. (2012), and Magdis et al. (2012b) for redshifts 0, 1, and 2. This table shows that the smallest distances are obtained when the Magnelli MS is adopted (points in Figs. 11 and 12), strengthening our conclusion.

The first parameter we consider is dust temperature. Magnelli et al. (2014) have shown that dust temperature increases with distance above the MS and as a function of redshift for a sample of galaxies with a wide range of stellar masses and SFRs from GOODS-N, GOODS-S and COSMOS from redshift 0 to ~2. Figure 11 shows the dust temperatures of LBAs, derived in the same way as for the galaxies in Magnelli et al. (2014, see Sect. 4.2), as a function of the LBA distances from the main sequences at $z = 0$, 1, and 2. The figure also shows the region occupied by the Magnelli et al. sample at all redshifts (blue solid box) and that occupied by a sample of low-metallicity lensed

[5] In order to be consistent with the dust to gas mass ratio we use, the metallicity should be derived from the method given in Pettini & Pagel (2004), which is the case for the metallicities we use for the LBAs as given in Overzier et al. (2009).

Table 8. Distances of LBAs from different definitions of main sequences (Magnelli et al. 2014; Magdis et al. 2012b; Speagle et al. 2014; Whitaker et al. 2012) at $z = 0$, 1 and; 2.

Name	z	Magnelli+14	Magdis+12	Speagle+14	Whitaker+12
005527	0	20.03	49.86	41.33	33.28
	1	3.88	7.66	3.42	2.94
	2	1.40	2.15	1.51	0.62
015028	0	12.14	23.23	38.70	23.47
	1	2.63	3.57	2.44	2.48
	2	1.13	1.00	0.99	0.63
021348	0	10.89	18.59	39.07	21.56
	1	2.56	2.86	2.25	2.42
	2	1.11	0.80	0.88	0.65
080844	0	6.56	15.76	14.67	11.27
	1	1.27	2.42	1.16	1.02
	2	0.48	0.68	0.51	0.22
082001	0	12.17	29.24	27.22	20.91
	1	2.37	4.49	2.15	1.90
	2	0.89	1.26	0.94	0.41
092159	0	6.61	9.26	27.60	13.22
	1	1.85	1.42	1.38	1.62
	2	0.76	0.40	0.52	0.48
093813	0	10.30	27.93	27.93	15.15
	1	2.05	4.29	4.29	1.22
	2	0.61	1.20	1.20	0.23
143417	0	1.66	2.50	6.62	3.32
	1	0.43	0.38	0.35	0.39
	2	0.18	0.11	0.13	0.11
210358	0	5.69	7.42	24.85	11.35
	1	1.70	1.14	1.19	1.43
	2	0.68	0.32	0.44	0.43

star-forming galaxies at $z \sim 3$ from Saintonge et al. (2013, red dashed box). LBAs could represent relatively low-mass galaxies above the local main sequence with high dust temperatures but still be in rough agreement with the galaxies above the main sequence at $z = 0$ in the Magnelli sample. If the main sequences at $z = 1$ and 2 are considered, LBAs have even higher temperatures than the Magnelli sample, but have very similar temperatures to those found for the lensed star-forming galaxies at $z \sim 3$ from Saintonge et al. (2013). Although we cannot discriminate between these two scenarios, we note that the metallicity range of LBAs is very similar to that of the high-z lensed star-forming galaxies. Moreover, with the exception of the very high dust temperature and metallicity galaxy SDSSJ080844 (Table 7), dust temperature of the LBAs roughly anti-correlates with metallicity for LBAs, in agreement with the results of Saintonge et al.

Figure 12 shows other parameters related to the ISM as a function of distance from the main sequence, for comparison with the similar diagrams in Magdis et al. (2012b, panels a–c), and Díaz-Santos et al. (2013, panel d). Panel a shows $\alpha_{\rm CO}$ calculated as a function of metallicity following the relation given in the previous section from Genzel et al. (2012); panel b shows SFE ($=L_{\rm IR}/M_{\rm H_2}$); panel c shows the $L_{\rm IR}/L_{\rm CO}$ ratio; and panel d shows the [CII]/$L_{\rm FIR}$ ratio.

In the first three panels, we plot (1) the values for the LBAs calculated with respect to the main sequence at $z = 0$, 1, and 2; (2) the regions occupied by the local and high-redshift MS galaxies (blue box) and the local ULIRGs and high-redshift SMGs (red box) from Magdis et al. (2012b); and (3) the best-fit and the $\pm 1\sigma$ values obtained from Magdis et al. for their full sample.

When we consider the LBA values with respect to the main sequence at $z = 0$, only the $L_{\rm IR}/L_{\rm CO}$ ratio follows the fit (panel c). In particular, all the LBA values have ratios similar to those observed in ULIRGs and SMGs. However, as shown in Fig. 9, at least two of the LBAs lie on the $L_{\rm IR} - L'_{\rm CO}$ relationship followed by the main sequence galaxies, and this is not reflected in panel c of Fig. 12. When we consider the values calculated with respect to the main sequence at $z > 1$, these two galaxies are within one σ of the Magdis relation, in agreement with the findings of Fig. 9.

In panels a and b, the values of LBAs calculated with respect to the local main sequence are outside the regions for both MS galaxies and ULIRGs/SMGs, while they agree with those derived taking the main sequence galaxies at high redshift as a reference.

Panel d of Fig. 12 shows the [CII]/FIR ratio as a function of distance from the main sequence, analogous to Fig. 7 of Díaz-Santos et al. (2013). These authors analyze a sample of local LIRGs from the Great Observatories All-sky LIRG Survey (GOALS) sample and show that there exists a relation between the position of the galaxies with respect to the main sequence and their [CII]/FIR ratio. Galaxies with sSFR greater than three times the sSFR of the local MS (vertical solid line in the figure) are starburst systems with high-efficiency star formation and a progressively low [CII]/FIR ratio. Galaxies are considered to be [CII]-deficient when their [CII]/FIR ratio is less than 10^{-3} (horizontal dotted line). Panel d of Fig. 12 also shows the fit obtained considering only the GOALS galaxies without known AGNs (solid blue diagonal line) and its $\pm 1\sigma$ uncertainties (gray solid lines).

The [CII]/FIR values of the LBAs relative to the local MS are higher than those of the GOALS galaxies at similar distances from the main sequence; alternatively, for a given

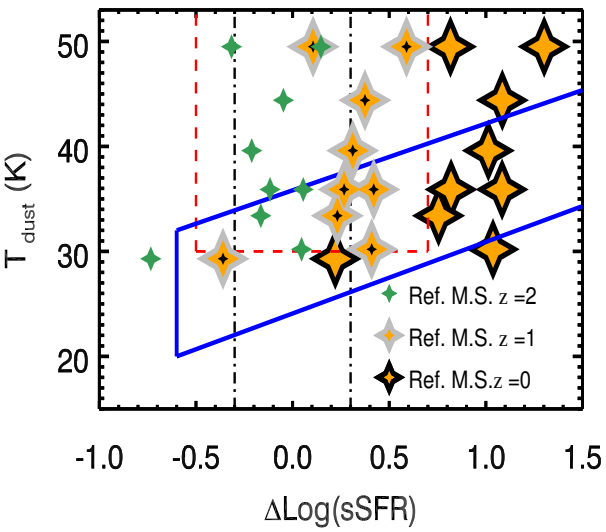

Fig. 11. LBAs on the relationship between their dust temperature and their distance from the main sequence at redshifts 0, 1, and 2, as indicated in the legend. We add the blue box enclosing the relation followed by a sample of galaxies from local to $z \sim 2$ presented by Magnelli et al. (2014) and, in red, the region occupied by a sample of $z \sim 3$ lensed low-metallicity star-forming galaxies presented by Saintonge et al. (2013).

[CII]/FIR ratio, LBAs seem to lie farther above the MS than the GOALS sample.

In this scenario LBAs seem to be extreme starburst galaxies with anomalously high [CII]/FIR ratios when compared to galaxies in the GOALS sample. We note that LBAs are also LIRGs, and therefore they match the GOALS sample in terms of infrared emission. In this scenario, LBAs would also have very low SFE ($L_{\rm IR}/M_{\rm H_2}$, panel b) for their starbursting nature. On the other hand, when the main sequence at $z = 1$ is considered, LBAs follow the fitted relation much better.

Díaz-Santos et al. (2013) show that [CII]/FIR ratio decreases with the compactness of the starburst traced by the FIR surface brightness ($\Sigma_{\rm IR} = L_{\rm IR}/{\rm Area}$). We have measured IR sizes as half light radii at 70 μm, for only four of our targets (Lutz et al. 2016). Díaz-Santos et al. (2013) calculate sizes using the half light radius in the MIR ($R_{\rm e,MIR}$). However, the bulk of the heating sources responsible for the emission at 70 μm and in the MIR should be sufficiently similar to allow a fair comparison. We find that the four LBAs for which we have reliable FIR sizes lie on the relation presented by these authors (their Fig. 5) with low FIR surface brightness ($\Sigma_{\rm IR} < 2 \times 10^{10}\ L_\odot\ {\rm kpc}^{-2}$), indicating that LBAs likely have extended star formation, as already suggested by the analysis of the $G_0/n_{\rm H}$ values in Sect. 5.2, and in agreement with their high [CII]/FIR ratio.

We conclude that LBAs represent a very peculiar local population with ISM properties very different from those of local galaxies in the same region of the M_*-*SFR* plane and with the same infrared emission. Indeed, the ISM properties of LBAs seem to be more similar to those of $z \sim 1$–2 main sequence galaxies. This result is consistent with the finding of Sect. 5.2, where we have shown that in LBAs, the physical parameters of the CNM are similar to those found in high-redshift galaxies rather than in local SFGs.

6.3. [CII] ALMA observations of main sequence galaxies at $z \sim 2$

We have shown that the ISM properties of LBAs are very similar to those of main sequence galaxies at higher redshifts. In light of this analogy we can use the observed [CII] fluxes of LBAs to predict how much time is necessary to observe [CII] in main sequence galaxies at $z = 2$ with ALMA.

The expected [CII] peak flux of a LBA redshifted to $z = 2$ ranges from ~10 to 50 mJy. This refers to the emission of the entire galaxy because LBAs are unresolved by PACS. We assume an intrinsic galaxy extent of ~6″, the typical Hα size of $z \sim 2$ main sequence galaxies. The time required to simply detect [CII] with ALMA with $S/N > 10$ and a velocity bin equal to 50 km s^{-1} is $\lesssim$2 h with 43 12 m antennae.

Assuming that the flux surface brightness decreases exponentially and matches the 70 km s^{-1} typical velocity resolution of Hα observations, the time required to map a $z = 2$ main sequence galaxy is 12–18 h depending on whether 50 or the current 43 offered antennae are considered.

We conclude that in its final state of development, ALMA will be able to detect a large number of relatively low-mass main sequence galaxies at $z = 2$ and to map a small subsample.

7. Summary and conclusions

We have presented an analysis of the neutral interstellar medium of a sample of Lyman-break analogs (LBAs) at $z \sim 0.2$ observed in [CII], [OI], and FIR continuum with the *Herschel*/PACS instrument and in the ^{12}CO(1–0) line with the IRAM PdBI. By definition, LBAs share many fundamental properties with Lyman-break galaxies at high redshift. All our targets are in the LIRG regime, but they have UV/FIR ratios much higher than LIRGs. The main goal of this paper is to investigate whether the ISM physical conditions in LBAs resemble those of their high-redshift analogs and thus to offer a unique reference sample for planning future submillimeter observations of high-redshifts star-forming galaxies. The main conclusions of this analysis are the following:

- We have detected all galaxies in line and FIR continuum emission. The atomic, molecular, and ionized gas share the same global kinematics as traced by the integrated line velocity dispersions. We have not detected outflows in the FIR fine structure lines, even in targets where high-velocity ionized gas outflows have been observed (Overzier et al. 2009; Heckman et al. 2011), possibly because the S/N of the FIR lines is too low to detect relatively faint line wings.
- By modeling the FIR [CII] and [OI] lines and TIR dust continuum as arising in PDRs, we show that the physical conditions of the neutral atomic gas in LBAs are relatively extreme with respect to the mean properties of local spiral galaxies: LBAs have lower gas temperatures and higher densities and pressures, similar to the conditions in high-redshifts star-forming galaxies. The $G_0/n_{\rm H}$ ratios of LBAs are lower than in local starbursts, analogous to what has been found in some high-redshift galaxies by Brisbin et al. (2015), and consistent with the interpretation that star formation in these galaxies is spread over several kpc and/or the gas density is higher than that in local SFGs. This interpretation is also supported by the low $\Sigma_{\rm IR}$ values (that trace starburst compactness) in at least four targets of our sample.
- LBAs do not suffer from the[CII]-*deficit* shown by infrared-bright galaxies, especially those with a significant AGN contribution. This is important for planning future observations of high-redshift main sequence galaxies with available submillimeter interferometers in the [CII] line.
- The [CII] emission of LBAs roughly follow the local HII-starburst [CII]-SFR relationship published by

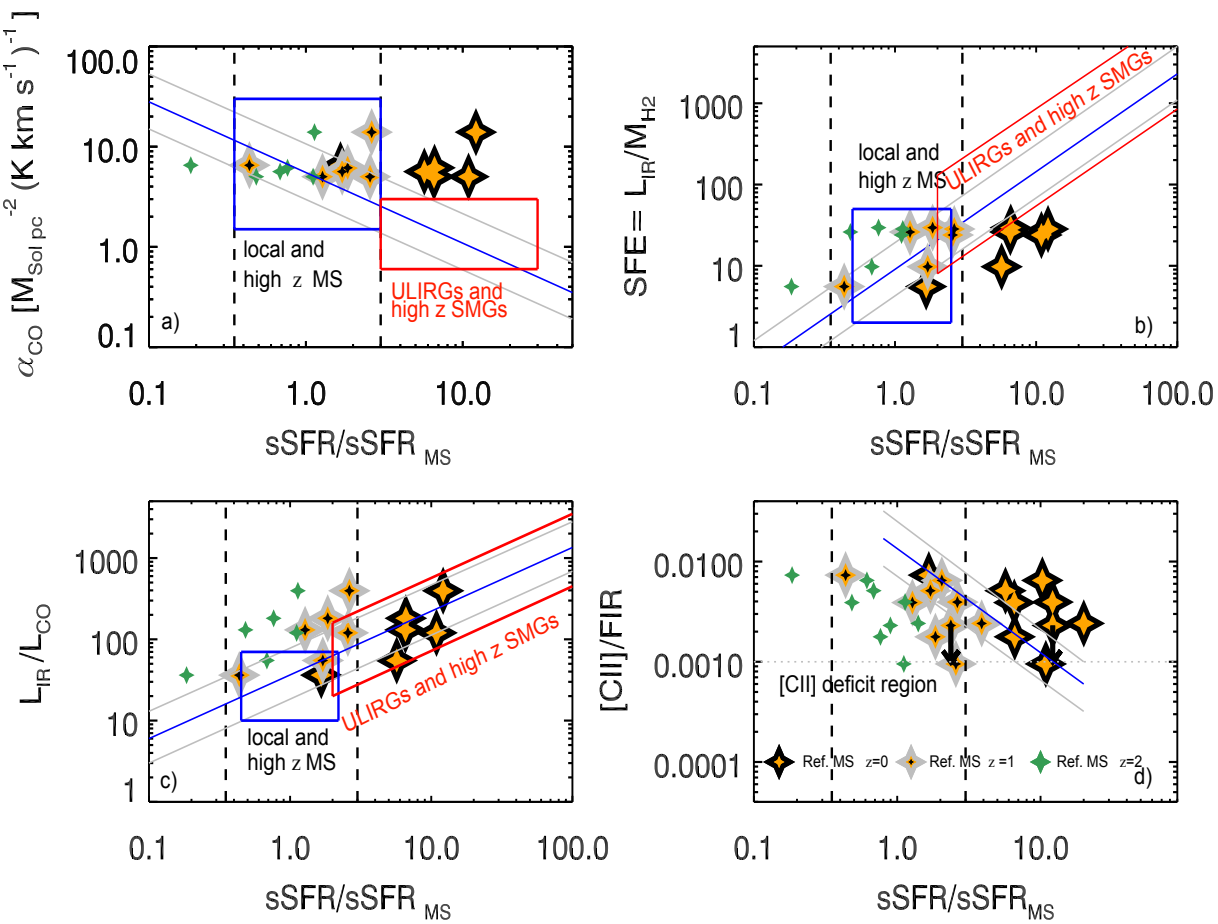

Fig. 12. LBA ISM parameters as a function of distance from the MS at $z = 0$, 1 and 2 (using the same symbols as in Fig. 11). The blue solid box represents the region occupied by SFGs on the MS and the red solid box that by galaxies above the MS.

De Looze et al. (2014). Despite the fact that LBAs show dense and warm gas similar to the gas in local dwarf galaxies, with which they also share stellar masses and metallicities, their [CII]/SFR ratio is higher than in local dwarfs, suggesting that LBAs belong to a distinct local population. We stress however, that the SFR-[CII] relationship has high dispersion, so SFRs cannot be derived with a precision better than a factor of ~3, and that the FIR continuum is a more efficient way to derive SFRs.

- The CO/FIR ratios of LBAs are typical of MS SFGs, except for two targets that lie on the merger sequence.
- We derive the total molecular gas fraction in LBAs with four methods, obtaining significantly higher fractions than in local SFGs with all methods except when ULIRG-like CO to H_2 conversion factors are used. This again strengthens the analogy between LBAs and high-redshift SFGs.
- LBAs lie above the local main sequence, but we find that, when their ISM properties are plotted as a function of their distance from the local MS, they do not lie in any of the regions occupied by other local samples. On the other hand, when the MS at $z > 1$ is considered, LBA values fall on the same regions occupied by high-redshift main sequence galaxies. This suggests that LBAs have ISM properties unique and never encountered in local galaxies above and on the MS, but similar to those of main sequence galaxies at high-redshift.

In summary, LBAs are distinct in their ISM properties from local spirals, dwarfs, and ULIRGs although they share some properties with each of these populations. Nevertheless, many ISM properties of LBAs are similar to those found in high-redshift main sequence galaxies. Therefore, we confirm that LBAs are, as in other respects, true analogs of these galaxies in their ISM properties as well.

In light of this conclusion, we have calculated the observing time needed to detect a typical Lyman-break galaxy (i.e., a high-redshift main sequence galaxy with $M_* \sim 10^{9.5-11}\ M_\odot$) at redshift 2 in [CII] with band 9 of ALMA. We find that one can detect such a target in a few hours with $S/N = 10$ and map it in 12−18 h (depending on the number of antennae).

Acknowledgements. The authors wish to thank the anonymous referee for their very useful comments and suggestions that improved the paper. PACS has been developed by a consortium of institutes led by MPE (Germany) and including UVIE (Austria); KU Leuven, CSL, IMEC (Belgium); CEA, LAM (France); MPIA (Germany); INAF-IFSI/OAA/OAP/OAT, LENS, SISSA (Italy); IAC (Spain). This development has been supported by the funding agencies BMVIT (Austria), ESA-PRODEX (Belgium), CEA/CNES (France), DLR (Germany), ASI/INAF (Italy), and CICYT/MCYT (Spain). A.J.B. acknowledges support from NFS grant AST-0955810. A. Verma acknowledges support from the Leverhulme Trust in the form of a Research Fellowship and a grant from the University of Oxford's Returning Carers Fund.

References

Abel, N. P., Dudley, C., Fischer, J., et al. 2009, ApJ, 701, 1147
Alexandroff, R., Overzier, R. A., Paragi, Z., et al. 2012, MNRAS, 423, 1325
Baldwin, J. A., Phillips, M. M., & Terlevich, R. 1981, PASP, 93, 5
Bañados, E., Decarli, R., Walter, F., et al. 2015, ApJ, 805, 8
Basu-Zych, A., Schiminovich, D. R., Johnson, B. D., et al. 2007, ApJS, 173, 457
Basu-Zych, A., Gonçalves, T. S., Overzier, R., et al. 2009, ApJ, 699, L118
Berta, S., Lutz, D., Genzel, R., et al. 2016, A&A, 587, A73

Béthermin, M. Daddi, E., Magdis, G., et al. 2015, A&A, 573, A113
Bigiel, F., & Blitz, L. 2012, ApJ, 756, 183
Bothwell, M. S., Aguirre, J. E., Aravena, M., et al. 2017, MNRAS, 466, 2825
Brisbin, D., Ferkinhoff, C., Nikola, T., et al. 2015, ApJ, 799, 13
Carilli, C. L., & Walter, F. 2013, ARA&A, 51, 105
Combes, F., García-Burillo, S., Braine, J., et al. 2013, A&A, 550, A41
Contursi, A., Poglitsch, A., Graciá Carpio, J., et al. 2013, A&A, 549, A118
Cormier, D., Madden, S. C., Lebouteiller, V., et al. 2015, A&A, 578, A53
Cox, D. 2005, ARA&A, 43, 337
Cresci, G., Hicks, E. K. S., Genzel, R., et al. 2009, ApJ, 697, 115
Daddi, E., Elbaz, D., Walter, F., et al. 2010a, ApJ, 714, 118
Daddi, E., Bournaud, F., Walter, F., et al. 2010b, ApJ, 713, 686
Dale, D. A., & Helou, G. 2002, ApJ, 576, 159
De Breuck, C., Williams, R. J., Swinbank, M., et al. 2014, A&A, 565, A59
De Looze, I., Cormier, D, Lebouteiller, V., et al. 2014, A&A, 568, A62
Díaz-Santos, T., Armus, L., Charmandaris, V., et al. 2013, ApJ, 774, 68
Downes, D., & Solomon, P. M. 1998, ApJ, 507, 615
Draine, B. T., & Li, A. 2007, ApJ, 657, 810
Draine, B. T., Dale, D. A., Bendo, G., et al. 2007, ApJ, 663, 866
Elmegreen, B. G., Bournaud, F., & Elmegreen, D. M. 2008, ApJ, 688, 67
Erb, D. K., Steidel, C., Shapley, A. E., et al. 2006a, ApJ, 646, 107
Erb, D. K., Shapley, A. E., Pettini, M., et al. 2006b, ApJ, 644, 813
Fabbiano, G., Krauss, M., Zeras, A., et al. 2003, ApJ, 598, 272
Fischer, J., Abel, A. P., González-Alfonso, E., et al. 2014, ApJ, 795, 117
Förster Schreiber, N. M., Genzel, R., Bouché, N., et al. 2009, ApJ, 706, 1364
Freundlich, J., Combes, F., Tacconi, L. J., et al. 2013, A&A, 553, A130
Glazebrook, K. 2013, PASA, 30, 56
Gallerani, S., Neri, R., Maiolino, R., et al. 2012, A&A, 543, A114
Genzel, R., Tacconi, L. J., & Graciá-Carpio, J. 2010, MNRAS, 407, 209
Genzel, R., Newman, S., Jones, T., et al. 2011, ApJ, 733, 101
Genzel, R., Tacconi, L., Combes, F., et al. 2012, ApJ, 746, 69
Genzel, R., Tacconi, L. J., Lutz, D., et al. 2015, ApJ, 800, 20
Goicoechea, J. R., Teyssier, D., Etxaluze, M., et al. 2015, ApJ, 812, 75
Gonçalves, T. S., Basu-Zych, A., Overzier, R., et al. 2010, ApJ, 724, 1373
Gonçalves, T. S., Basu-Zych, A., Overzier, R., et al. 2014, MNRAS, 442, 1429
González-Alfonso, E., Smith, H. A., Ashby, M. L. N., et al. 2008, ApJ, 675, 303
González-Alfonso, E., Fischer, J., Sturm, E., et al. 2015, ApJ, 800, 69
Graciá Carpio, J., Sturm, E., Hailey-Dunsheath, S., et al. 2011, ApJ, 728, L7
Guilloteau, S., Delannoy, J., Downes, D., et al. 1992, A&A, 262, 624
Guilloteau, S., & Lucas, R. 2000, ASP Conf. Proc. 217, eds. J. G. Magnum, & S. J. E. Radford, 299
Hailey-Dunsheath, S., Nikola, T., Stacey, G. J., et al. 2010, ApJ, 714, L162
Heckman, T. M., Hoopes, C. G., Seibert, M., et al. 2005, ApJ, 619, L35
Heckman, T. M., Borthakur, S., Overzier, R., et al. 2011, ApJ, 730, 2011
Helou, G., Khan, I. R., Malek, L., et al. 1988, ApJS, 68, 151
Herrera-Camus, R., Bolatto, A. D., Wolfire, M., et al. 2015, ApJ, 800, 1
Herrera-Camus, R., Bolatto, A. D., Wolfire, M., et al. 2017, ApJ, 835, 201
Hollenbach, D. J., & McKee, C. F. 1989, ApJ, 342, 306
Hoopes, C. G., Heckman, T. M., Salim, S., et al. 2007, ApJS, 173, 441
Ibar, E., Lara-López, M. A., Herrera-Camus, R., et al. 2015, MNRAS, 449, 2498
Inami, H., Armus, L., Charmandaris, V., et al. 2013, ApJ, 777, 156
Jankins, E. B., & Tipps, T. M. 2011, ApJ, 734, 65
Janssen, A. W., Christopher, N., Sturm, E., et al. 2016, ApJ, 822, 43
Kaufman, M. J., Wolfire, M. G., Hollenbach, D. J., et al. 1999, ApJ, 527, 795
Kennicutt, R. C., Jr, & Evans, N. J. 2012, ARA&A, 50, 531
Kroupa, P., & Weidner, C. 2003, ApJ, 598, 1076
Law, D. R., Steidel, C. C., Erb, K. D., et al. 2007, ApJ, 669, 929
Li, A., & Draine, B. T. 2001, ApJ, 554, 778
Lian, J. H., Li, J. R., Yan, W., & Kong, X. 2015, MNRAS, 446, 1449
Luhman, M. L., Satyapal, S., Fischer, J., et al. 2003, ApJ, 594, 758
Lutz, D., Berta, S., Contursi, A., et al. 2016, A&A, 591, A136
Magdis, G. E., Daddi, E., Sargent, M., et al. 2012a, ApJ, 758, L9
Magdis, G. E., Daddi, Béthermin, M., et al. 2012b, ApJ, 760, 6
Magdis, G. E., Rigopoulou, D., Hopwood, R., et al. 2014, ApJ, 796, 63
Magnelli, B., Lutz, D., Saintonge, A., et al. 2014, A&A, 561, A86
Maiolino, R., Caselli, P., Nagao, T., et al. 2009, A&A, 500, L4
Maiolino, R., Gallerani, S., Neri, R. 2012, MNRAS, 425, 66
Maiolino, R., Carniani, S., & Fontana, A. 2015, MNRAS, 452, 54
Malhotra, S., Kaufman, M. J., Hollenbach, D., et al. 2001, ApJ, 561, 766
Negishi, T., Onaka, T., Chan, K.-W., et al. 2001, A%A, 357, 566
Newman, S. F., Genzel, R., Förster-Schreiber, N. M., et al. 2012a, ApJ, 761, 43
Newman, S. F., Shapiro Griffin, G. K., Genzel, R., et al. 2012b, ApJ, 752, 111
Overzier, R. A., Heckman T. M., Kauffmann, G., et al. 2008, ApJ, 667, 37
Overzier, R. A., Heckman T. M., Tremonti, C., et al. 2009, ApJ, 706, 203
Overzier, R. A., Heckman, T. M., Schiminovich, D., et al. 2010, ApJ, 710, 979
Overzier, R. A., Heckman, T. M., Wang, J., et al. 2011, ApJ, 726, L7
Pentericci, L., Carniani, S., Cstellano, M., et al. 2016, ApJ, 829, L11
Pettini, M., & Pagel, B. E. J. 2004, MNRAS, 348, L59
Pilbratt, G. L., Riedinger, J. R., Passvogel, T., et al. 2010, A&A, 518, L1
Poglitsch, A., Waelkens, C., Geis, N., et al. 2010, A&A, 518, L2
Saintonge, A., Kauffmann, G., Kramer, C., et al. 2011, MNRAS, 415, 32
Saintonge, A., Lutz, D., Genzel, R., et al. 2013, ApJ, 778, 2
Salmon, B., Papovich, C., & Finkelstein, S. L. 2015, ApJ, 799, 183
Schaerer, D., Boone, F., Jones, T., et al. 2015, A&A, 576, A2
Speagle, J. S., Steinhardt, C. L., Capak, P. L., et al. 2014, ApJS, 214, 15
Stacey, G. J., Hailey-Dunsheath, S., Ferkinhoff, C., et al. 2010, ApJ, 724, 957
Steidel, C. C., Giavalisco, M., Dickinson, M., et al. 1996, AJ, 112, 352
Steidel, C. C., Rudie, G. C., Strom, A. L., et al. 2014, ApJ, 795, 165
Swinbank, A. M., Papadopoulos, P. P., & Cox, P. 2011, ApJ, 742, 11
Swinbank, A. M., Smail, I., Sobral, D., et al. 2012, ApJ, 760, 130
Tacconi, L. J., Genzel, R., Neri, R., et al. 2010, Nature, 463, 781
Tacconi, L. J., Neri, R., Genzel, R., et al. 2013, ApJ, 768, 74
U, V., Sanders, D. B., Mazzarella, J. M., et al. 2012, ApJS, 203, 9
van Moorsel, G., Kemball, A., & Greisen, E. 1996, ADASS, ASP Conf. Ser., 101, 37
Veilleux, S., & Osterbrock, D. E. 1987, ApJS, 63, 295
Venemans, B. P., McMahon, R. G., Walter, F., et al. 2012, ApJ, 751, L25
Zhao, Y., Yan, L., & Tsai, C. 2016, ApJ, 824, 2016
Wagg, J., Wiklind, T., Carilli, C., et al. 2012, ApJ, 752, L30
Wang, R., Waag, J., Carilli, C., et al. 2013, ApJ, 773, 44
Whitaker, K. E., van Dokkum, P. G., Brammer, G., & Franx, M. 2012, ApJ, 754, L29
Wisnioski, E., Førster-Schreiber, N., Wuyts, S., et al. 2015, ApJ, 799, 209
Yun, M. S., Aretxaga, I., & Gurwell, M. A. 2015, MNRAS, 454, 3485